A Path to Configurable Solid State Transformers and Energy Routers: Introduction to Modular Active Cell Control

Raffael Schwanninger, *Student Member, IEEE*, Niklas Stöcklein, Nikolai Weitz, Xiaotian Yang, and Martin März

***Abstract*—This article introduces a control strategy for a modular multiactive bridge architecture that extends the single phase shift as a novel approach to enable fully decentralized control of the modular active cell (MAC) on a single, arbitrarily large multiwinding transformer. The MAC aims to provide a fully modular, configurable, and scalable solution for solid state transformers and energy routers, enabling full power and voltage variability in isolated interconnections of diverse dc networks. A novel modeling approach based on discrete-time state-space is introduced. The model is verified through measurements and simulation, showing high accuracy and prediction capability.**

***Index Terms*—Multiactive bridge (MAB), multi-input–multi-output (MIMO), multicell, multiport energy router, power electronics building block, solid state transformer (SST).**

I. Introduction

THE global energy landscape is undergoing a significant transformation, marked by the increasing adoption of direct current (dc) networks across various sectors. Applications such as electric vehicle (EV) fast-charging [1], [2], [3], data centers [4], [5], [6], naval electrification [7], [8], [9], renewable energy integration [10], [11], [12], industrial automation [13], [14], [15], and intelligent medium voltage direct current (MVDC) distribution grids [16], [17], [18] are driving the demand for efficient and flexible dc power distribution systems. These dc networks offer advantages in terms of efficiency and compatibility with modern electronic loads as well as higher cost efficiency in distribution [19], [20], [21]. Although all of these applications are similar, they vary greatly in terms of voltage and power requirements. To enable a swift transition to renewable energies, modular solutions are therefore necessary to limit the required engineering effort. Thus, there is a pressing need for advanced power electronic architectures that can provide configurable, efficient, and isolated capabilities to facilitate the seamless integration and operation of diverse dc networks [22], [23].

The simplest case of this modularity can be found in power electronic building blocks (PEB), which were introduced to focus on the optimization of only a few identical building blocks, enabling faster and more efficient design of power systems [24], [25]. An early example is [26], where a PEB is developed to simplify the need for external communication and synchronization in bidirectional switches in matrix converters. The concept of modularity is extended in [27] with the modular multilevel converter (MMC). For the MMC, modularity allows for voltage and power scalability in conversion from ac to dc through identical sub-modules. Depending on configuration, these sub-modules allow high blocking voltages through serialization, or high currents through parallelization. To allow for galvanic isolation and high conversion ratios, this modular sub-module approach has been applied to solid state transformers (SST) as well [28], [29], [30], [31], [32]. To enable the direct connection of low voltage direct current (LVDC) to MVDC, a connection to a transformer can be added to each MMC module. The modules can either be connected to LVDC with multiple transformers, or with a single large transformer connecting all modules to multiple LVDC ports. As shown in [33], the benefits of a shared transformer are better voltage balancing, higher power density, and a generally higher efficiency.

On the other side of the power and voltage spectrum, multiport converters or energy routers are investigated in [34], [35], [36], [37], [38], [39], these allow for multiple input multiple output (MIMO) connection of renewable energy sources and storage systems to dc microgrids. The cells of this MIMO converter are reconfigurable, allowing for serialization and parallelization to realize different voltage and current specifications. This allows for a single optimized power electronics design to be applied to diverse applications such as server racks [40], modular battery storage [41], vehicular applications [35], and renewable energy systems [42].

Although many different topologies for use in more or less modular concepts exist [34], dual active bridge (DAB) based

Received 25 June 2025; revised 12 September 2025; accepted 12 October 2025. Date of publication 15 October 2025; date of current version 19 January 2026. This work was conducted within the project ECS4DRES. ECS4DRES is supported by the Chips Joint Undertaking under Grant 101139790 and its members, including the top-up funding by Germany, Italy, Slovakia, Spain, and The Netherlands. Recommended for publication by Associate Editor D. O. Neacsu. *(Corresponding author: Raffael Schwanninger.)*

Raffael Schwanninger, Niklas Stöcklein, Nikolai Weitz, and Martin März are with the Institute of Power Electronics, Friedrich-Alexander-University, 90429 Nuremberg, Germany (e-mail: raffael.schwanninger@fau.de; niklas.stoecklein@fau.de; nikolai.weitz@fau.de; martin.maerz@fau.de).

Xiaotian Yang is with the Fraunhofer Institute for Integrated Systems and Device Technology IISB, 91058 Erlangen, Germany (e-mail: xiaotian.yang@iisb.fraunhofer.de).

Color versions of one or more figures in this article are available at https://doi.org/10.1109/TPEL.2025.3621885.

Digital Object Identifier 10.1109/TPEL.2025.3621885

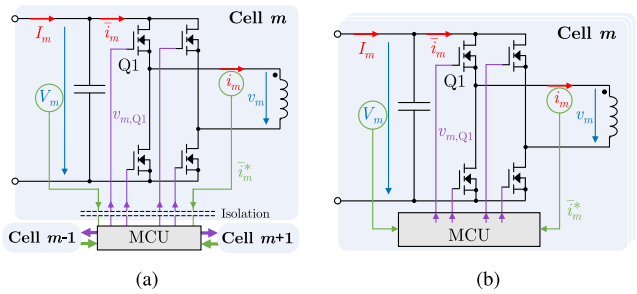

Fig. 1. Control strategy of an MAB: Placement of the MCU. (a) Conventional: Centralized. (b) Proposed: Decentralized.

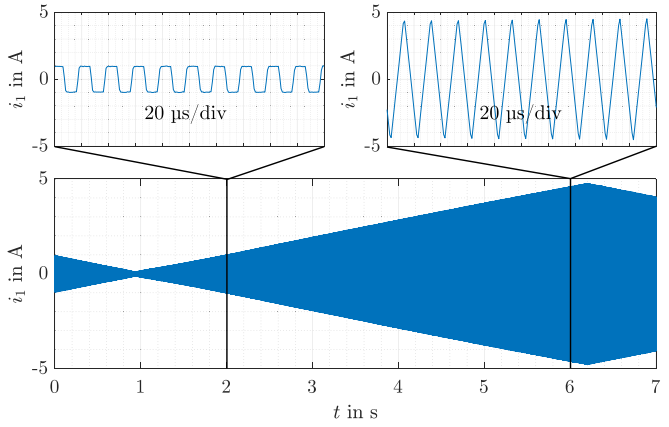

Fig. 2. Experimentally measured DAB transformer current with implemented single phase shift without a central control unit.

solutions, as initially introduced in [43], are prime candidates due to their bidirectionality and ease of control. If more than two active bridges are connected to a multiwinding transformer, the DAB becomes a multi-active bridge (MAB). One cell of such an MAB is shown in Fig. 1. Whether the MAB is used on energy routers [37], [38] or SSTs [33], all cells require a central control unit (MCU), which sets the phase-shifts between all connected cells. As indicated in Fig. 1(a), this MCU therefore needs to communicate control signals to the cells. These need to be calculated accordingly from the voltage and possibly even current measurements within each cell. Therefore, measurement signals need to be measured locally and fed back to the central MCU. In terms of modularity, this centralized control is unfavorable, since each added cell increases the load on the MCU. In addition, the necessary wiring to connect all modules to one controller scales likewise with the number of modules. In MVDC applications, costly signal transmission over MV isolation barriers needs to be implemented to maintain the galvanic isolation, adding additional cost for the low latency communication required [44], [45].

Ideally, each cell would be controlled by its own MCU as shown in Fig. 1(b). This MCU controls the cell locally, generating gate signals based on the cells measured voltage and current. The only communication to other cells or a central controller would be through the exchange of slow moving set-values where the increased delay of cost effective solutions [46] does not matter for primary control stability. While distributed control with primary local controllers have been investigated [47], [48], SSTs with DABs still need to break the primary to secondary side isolation barrier with low latency.

This necessity can easily be showcased by two cells, each controlled by its own MCU connected to form a DAB. Fig. 2 shows the measured transformer current of a DAB in the case of a decentralized control strategy with an initially fixed phase shift of approx 20°. While this phase shift might be initially constant between switching cycles, even minute differences in the MCUs local oscillators will lead to the two cells eventually de-synchronizing. In consequence, the phase shift increases linearly with no stable operating point (OP). Furthermore, even setting an initial phase shift is not easily possible, as there is no information shared regarding the phase of the two cells. This effect is worsened in an MAB, as all cells will de-synchronize, requiring some external primary controller to keep all cells in lock-step.

To reduce or even fully mitigate the need for any external communication, this article introduces a control strategy that extends the single phase shift as a novel approach to enable a fully modular multi-active bridge (MMAB). The MMAB consists of modular active cells (MAC), which can operate independently on a shared transformer. The MAC aims to provide a modular, configurable, and scalable solution for SSTs and energy routers, enabling efficient and isolated interconnection of diverse dc networks. Instead of controlling the current flow from cell to cell by setting a phase shift, the switching frequency of each MAC is varied slightly based on its local control law. This frequency variation then induces a phase shift between the MAC and all other MAC on the transformer. To allow designers to design stable local control, we develop a discrete-time state-space model for the MAC on a multiwinding transformer. Although discrete-time models have been developed before for general power converters [49], [50], [51], [52], [53], [54] as well as DAB [55], [56], [57], [58], [59], [60], the model developed in this article does not use averaging of continuous-time models, but rather develops the discrete-time model ab initio, as it directly results from the digital control method.

The main contribution of this article can be summarized as follows:

1) The introduction of MAC control.
2) The description of the MMAB with a linear discrete-time state-space model.
3) Introduction of a stability criterion for an MMAB under MAC control.
4) Identification of causes for instability.

As many readers might not be familiar with the discrete-time state-space approach, this article introduces the basic and simplified control strategy independent of the modeling in Section II. The individual sections of Section III will introduce the intended control scheme alongside the discrete-time state-space model step by step with increasing complexity. Measurement results are shown for each step to act as verifications, as well as examples. Section IV finally acts as a full verification of the developed

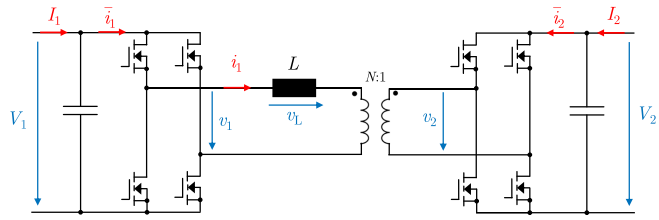

Fig. 3. Lossless equivalent circuit of a DAB with definitions of voltages and currents.

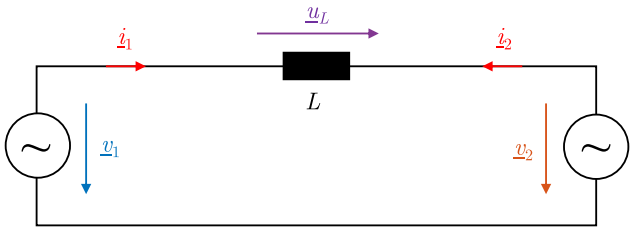

Fig. 4. First harmonic approximation of a DAB with $N = 1$.

model. As this article is intended to introduce the fundamentals of MAC control, topics concerning efficiency optimization, ideal transformer design, or even regular operation in SST or energy router applications are not extensively studied in this article. Section V therefore discusses some of the many questions that remain open before the MMAB can be used effectively in any of its intended applications.

II. Fundamentals of MAC Control

Before developing the complete control for the MAC in Section III, this section should act as a simplified introduction to the control scheme. Therefore, the basic control strategy is explained using a DAB, which is shown in Fig. 3 as a simplified and lossless equivalent circuit. The phase shift between both full bridges is given by (1) with t_1 and t_2 being the points in time of the rising edge of v_1 and v_2, respectively. T_s is the time of a switching period

$$\varphi_{12} = \varphi_1 - \varphi_2 = (t_2 - t_1) \cdot \omega_\mathrm{s} \tag{1}$$

$$\omega_\mathrm{s} = \frac{2\pi}{T_\mathrm{s}} = 2\pi f_\mathrm{s}. \tag{2}$$

The power transfer from cell 1 to 2 and the current $\bar{i}_1$ is determined by (3) and (4), respectively, both having a parabolic dependency on φ_{12}

$$P_{12} = \frac{V_1 \cdot NV_2}{\omega_\mathrm{s} \cdot L} \cdot \varphi_{12} \cdot \left(1 - \frac{|\varphi_{12}|}{\pi}\right) \tag{3}$$

$$\bar{i}_1 = \frac{NV_2}{\omega_\mathrm{s} \cdot L} \cdot \varphi_{12} \cdot \left(1 - \frac{|\varphi_{12}|}{\pi}\right). \tag{4}$$

To explain the control principle, Fig. 3 can be simplified using the first harmonic approximation (FHA) as shown in Fig. 4. To simplify the equations, N should be equal to 1. The fundamental frequency equals the initial switching frequency ω_0. Furthermore, using complex values in a coordinate system

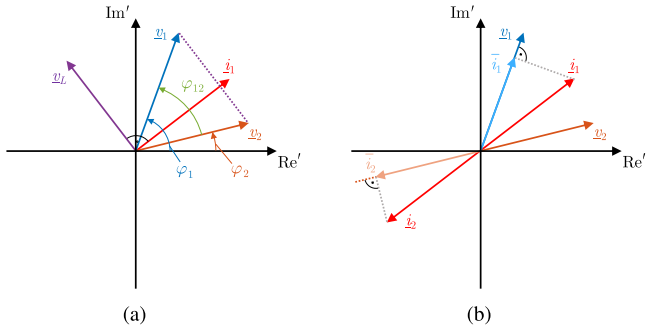

Fig. 5. Voltage-phasors $\underline{v}_1$ and $\underline{v}_2$ of a DAB in the rotating complex plane Re′ and Im′ using the FHA at an arbitrary phase angle φ_{12}. The measured active currents are projections of the complex $\underline{i}_1$ and $\underline{i}_2$ onto their respective voltages. (a) Voltage and current phasors. (b) Obtaining the active current.

that rotates with ω_0 defined by

$$\mathrm{Re}'(\underline{v}) = \mathrm{Re}(\underline{v}) \cdot \mathrm{e}^{j\omega_0 t} \tag{5}$$

and

$$\mathrm{Im}'(\underline{v}) = \mathrm{Im}(\underline{v}) \cdot \mathrm{e}^{j\omega_0 t} \tag{6}$$

oscillations with ω_0 can be described as a phasor at a fixed phase angle. An arbitrary state of the DAB with power transfer from v_1 to v_2 is shown in Fig. 5(a). The voltages are depicted as complex phasors $\underline{v}_1$ and $\underline{v}_2$. If $\underline{v}_1$ and $\underline{v}_2$ are inequal in phase or length, the complex currents $\underline{i}_1$ and $\underline{i}_2$ are nonzero. For the proposed control scheme, the active current $\bar{i}_m$ at each cell is of interest. In the phasor diagram, the active currents $\bar{i}_1$ and $\bar{i}_2$ can therefore be determined as the projection of the complex currents $\underline{i}_1$ and $\underline{i}_2$ onto their respective voltages, as depicted in Fig. 5(b).

The fundamental principle of the proposed control strategy is based on changing the phase angle of the phasors by adjusting $\omega_{\mathrm{s},m}$ of cell m. The assumption for this is, that a current $\bar{i}_m^*$ can be measured, which represents $\bar{i}_m$ sufficiently as explained later in Section III-A. Because of

$$\dot{\varphi}_m = \frac{\mathrm{d}\varphi_m}{\mathrm{d}t} = \omega_{\mathrm{s},m} \tag{7}$$

the desired phase shift and therefore the state of the DAB can be achieved by

$$\dot{\varphi}_{12} = \frac{\mathrm{d}\varphi_{12}}{\mathrm{d}t} = \omega_{\mathrm{s},1} - \omega_{\mathrm{s},2}. \tag{8}$$

Thus, a change in phase is obtained by integration of the difference in frequency. A control loop with a P controller with a constant gain K_P can be formed as shown in Fig. 6, which here is referred to as the source control. This controller adjusts the $\omega_{\mathrm{s},m}$ of its own cell m from an offset value ω_0 based on the measured current $\bar{i}_m^*$ and a set value $i_{\mathrm{set},m}$

$$\omega_{\mathrm{s},m} = \omega_0 + K_\mathrm{P} \cdot (i_{\mathrm{set},m} - \bar{i}_m^*). \tag{9}$$

The DAB itself can be modeled as a subtraction of angular frequencies followed by an integration to obtain the phase-shift and the DAB transfer function (4). The DAB transfer function outputs the transformer current $\bar{i}_1$ as a change in the OP of the DAB. Implementing this control on both sides of the DAB in

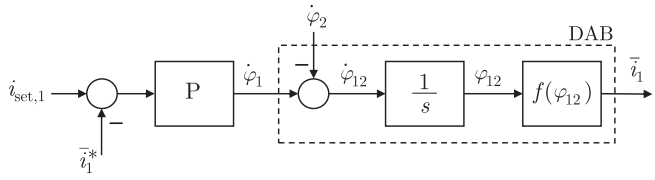

Fig. 6. Source control loop with a P controller. The DAB can be modeled as a frequency integrator leading to a change in phase and a nonlinear function translating phase to active current. $\dot{\varphi}_1$ and $\dot{\varphi}_2$ represent the change in phase due to the switching frequency of cells 1 and 2.

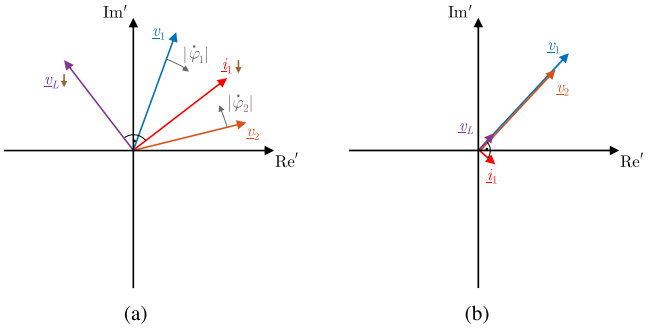

Fig. 7. Phasors of two cells in source control. The measured currents will lead to frequency adjustments (gray arrows). The change in frequency moves $\underline{v}_1$ and $\underline{v}_2$ closer, reducing φ_{12}. In steady state, both $\underline{v}_1$ and $\underline{v}_2$ are in phase and no active current is transferred. (a) Initial state. (b) Steady state.

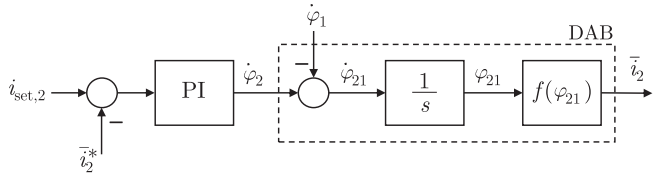

Fig. 8. Load control loop consisting of a PI controller and DAB model.

Fig. 4 with a setpoint of 0 A results in decreasing φ_1 due to the negative error [see Fig. 7(a)]. φ_2 is increased, respectively. This concludes in a reduction of φ_{12} until the steady state [see Fig. 7(b)] is reached with

$$\dot{\varphi}_{12} = \varphi_{12} = 0. \tag{10}$$

Both full bridges are switching synchronously with f_s. In this case, no active power is transmitted

To achieve stationary accuracy with one full bridge at a defined current, it is necessary to implement a PI controller with an additional integrator gain K_I

$$\omega_{\mathrm{s},m} = \omega_0 + K_\mathrm{P} \cdot (i_{\mathrm{set},m} - \bar{i}_m^*) + K_\mathrm{I} \int (i_{\mathrm{set},m} - \bar{i}_m^*)\mathrm{d}t. \tag{11}$$

This control loop can be interpreted as load control and shown in Fig. 8.

Implementing this controller on the $\underline{v}_2$ side of Fig. 4 with a setpoint of $\bar{i}_{\mathrm{set},2} < 0\,\mathrm{A}$ and the starting point of synchronous full bridges [see Fig. 7(b)] results in the response shown in Fig. 9(a). The full bridge represented by $\underline{v}_1$ remains with source control. Therefore, φ_2 is decreased by the PI controller. Because

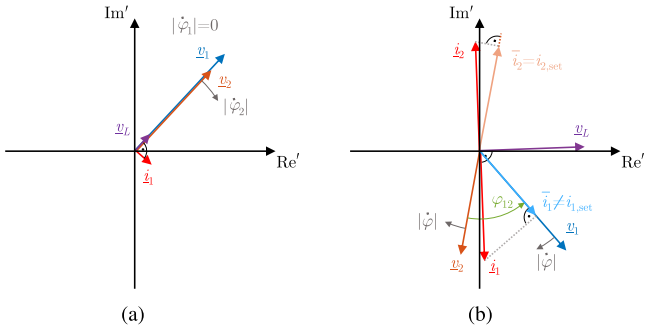

Fig. 9. Principle of load control at full bridge 2 (source control at full bridge 1). Load control will force a constant φ_{12} to maintain a $\bar{i}_2$. In steady state (b), all phasors rotate at a fixed frequency in the itself rotating coordinate system, resulting in a change of switching frequency depending on the load current. (a) Reaction of controller. (b) Steady state: Constant rotation with $|\dot{\varphi}|$.

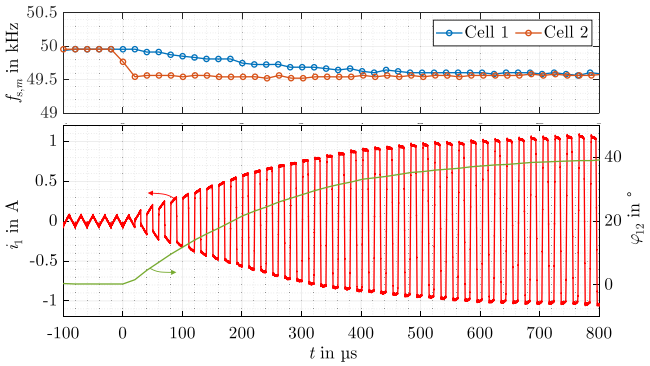

Fig. 10. Experimentally measured current of a DAB configuration with cell 1 and cell 2 as source and load control, respectively. Frequencies and phase shift are calculated from the measured gate signals $v_{1,\mathrm{Q1}}$ and $v_{2,\mathrm{Q1}}$.

of the integral part the PI controller ensures stationary accuracy. $\omega_{\mathrm{s},2}$ will therefore stay different from ω_0 even if no remaining error is present. At $\underline{i}_1$ the error remains such that φ_1 is reduced constantly. All phasors rotate with a fixed frequency within the itself rotating coordinate system. Fig. 9(b) shows this rotating steady state at an arbitrary point in time. While the switching frequency f_s is lower than the initial switching frequency $f_{\mathrm{s},0}$, the phase shift φ_{12} remains constant. In contrast to (10), with load control, the phase shift is

$$\varphi_{12} \neq 0. \tag{12}$$

However, since

$$\dot{\varphi}_1 = \dot{\varphi}_2 = \dot{\varphi} \tag{13}$$

following equation must hold:

$$\dot{\varphi}_{12} = 0. \tag{14}$$

Fig. 10 shows an exemplary experimentally measured behavior of a DAB in source and load control. Cell 1 and cell 2 are configured with a source (setpoint to 0 A) and load control, respectively. To the zero point in time, the set point of the load steps from 0 A to −1 A. Due to the control error, cell 2 adapts its phase with the change of frequency (7). Therefore, a difference in the frequencies is present as shown in Fig. 10, which leads to

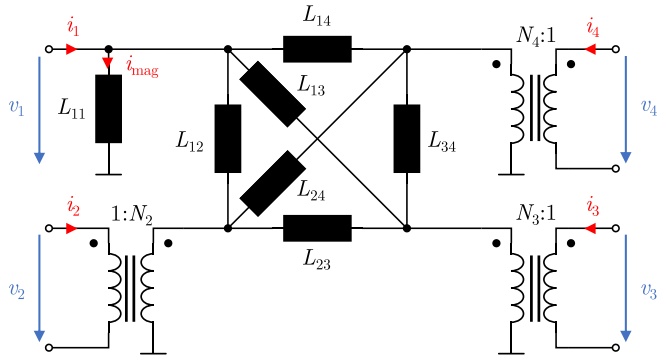

Fig. 11. ECM for a transformer with four windings/cells. Each interconnection of two cells is characterized by a stray inductance L_{ab}. The magnetizing inductance of all cells are included in L_{11}.

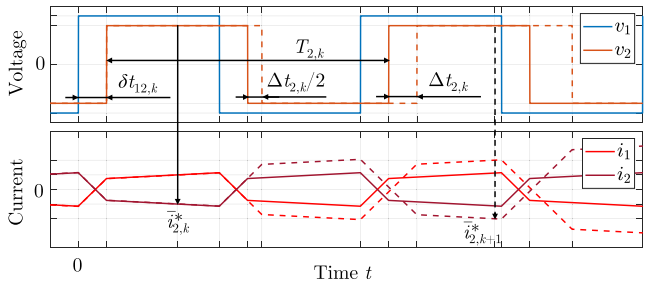

Fig. 12. Fundamental waveforms of a two cell MMAB. The sampling in cell 2 is indicated by the vertical black arrows. The phase shift $\delta t_{12,k}$ is adjusted by this sampled current through prolonging both half-waves by $\Delta t_{2,k}/2$.

a change in the phase shift (8) and in turn also in the transferred current (4). In steady state, (12), (13), and (14) are valid.

As the control scheme is based on both cells constantly changing their frequency to control the current, a slight offset in clock frequency in the respective controllers has little effect. Therefore, the control can be fully decentralized. Communication of the state of the DAB is transmitted by the transformer current. The control strategy can also be extended on multiwinding transformers, as explained in the next section. The closest analogy to MAC control is the operation of synchronous generators (SG) in an ac grid. With SGs the phase shifts and power transfer are induced by slight variations in rotational frequency as a result of loading. For the MMAB, the switching frequency therefore plays a role very similar to the rotational frequency of an SG, changing phase shifts and again power flow based on measured current.

III. Discrete-Time Modeling of an MMAB System

To determine stable control parameters for each cell, a state-space model of the MMAB is required. In this article, the transformer is described by the Extended Cantilever Model (ECM) as described in [61], as it is often used in multiport transformers [37], [38], and shown for a four cell transformer in Fig. 11. In the ECM, each cell a is connected to all other cells b through an inductance L_{ab}. Transformation ratios are included as N_a in each cell, apart from cell 1, where N_1 can be set to 1. The magnetizing inductance of all cells is included in L_{11}. The magnetizing inductance L_{aa} as seen from any other cell a needs to be calculated from L_{11}, N_a and the series parallel connection of all paths from cell a to cell 1. The total magnetization current i_{mag} is therefore the sum of the individual magnetization currents i_{mm} of all cells on an M-winding transformer

$$i_{\text{mag}} = \sum_{m=1}^{M} i_{mm}. \tag{15}$$

An M-winding transformer can be described as a simple linear time-invariant (LTI) system, with interconnections between each winding. The following sections will therefore deal with modeling the nonlinear time-variant active bridges on the LTI transformer. As the analysis behind the control scheme might not be trivial to every reader, we will introduce it step by step during the next sections. The final control scheme and accompanying model are given in Section III-E.

A. State-Space Model of Active Currents in Trapezoidal Mode

As explained in Section II, each cell of the MMAB should be controlled by its active input current $\bar{i}$. As $\bar{i}_a$ is not directly measurable by cell a, the MAC control instead relies on sampling the transformer current i_a at least once every switching period, as indicated in Fig. 12. For the following sections, each switching period will be referenced by an index k. Sampling the current in each half period will be introduced in Section III-E.

The resulting current $\bar{i}^*_{a,k}$ measured, is the sum of the currents from a to every other cell

$$\bar{i}^*_{a,k} = \sum_{m=1}^{M} \bar{i}^*_{am,k}. \tag{16}$$

The magnetization inductance is not included in the considerations for this section. Therefore,

$$\bar{i}^*_{aa} = 0 \tag{17}$$

is applied. For the following section, all cells are assumed to be operating in trapezoidal mode, which is defined as the absolute values of the phase angles between all cells are lower than $\pi/2$. If i_a is therefore sampled exactly at the center of the first half-cycle in the period k – as indicated by the black arrow in Fig. 12 for cell 2 – the individual currents between the cells a and b can be written as follows:

$$\bar{i}^*_{ab,k} = \frac{N_a N_b V_b}{L_{ab}} \cdot \delta t_{ab,k}. \tag{18}$$

We call $\bar{i}^*_{ab,k}$ the *dressed active currents*, as they are a representation of the *bare active currents* $\bar{i}_{ab,k}$. Compared to $\bar{i}_{ab,k}$ in (4), $\bar{i}^*_{ab,k}$ is calculated with the absolute time lag/lead $\delta t_{ab,k}$ between two phases, as phase angles φ_{ab} and angular frequencies ω_s are ill defined in variable frequency operation. Unlike centralized control schemes $\delta t_{ab,k}$ is adjusted by cells a and b through each cell changing its own cycle duration $T_{a,k}$ and $T_{b,k}$ by $\Delta t_{a,k}$ and $\Delta t_{b,k}$, respectively. This results in a changed $\bar{i}^*_{ab,k+1}$ at the next

sampling

$$\bar{i}^*_{ab,k+1} = \bar{i}^*_{ab,k} - \frac{N_a N_b V_b}{L_{ab}} \cdot (\Delta t_{a,k} - \Delta t_{b,k}). \tag{19}$$

This effect is depicted by the dashed lines in Fig. 12. Assuming a simple proportional controller with gain $K_{\mathrm{P},a}$ in cell a, $\Delta t_{a,k}$ will be determined from the sum of all partial currents and the cells set current value $i_{\mathrm{set},a,k}$

$$\Delta t_{a,k} = -K_{\mathrm{P},a} \cdot \left(i_{\mathrm{set},a,k} - \sum_{m=1}^{M} \bar{i}^*_{am,k} \right). \tag{20}$$

The (16), (19), and (20) can therefore be reformulated as a discrete-time state-space representation consisting the state transition matrix $\mathbf{A}$ for the state vector and the input matrix $\mathbf{B}$ for the set-point vector

$$\begin{pmatrix} \bar{i}^*_{1,k+1} \\ \bar{i}^*_{2,k+1} \\ \cdots \\ \bar{i}^*_{M,k+1} \end{pmatrix} = \mathbf{A} \begin{pmatrix} \bar{i}^*_{1,k} \\ \bar{i}^*_{2,k} \\ \cdots \\ \bar{i}^*_{M,k} \end{pmatrix} + \mathbf{B} \begin{pmatrix} i_{\mathrm{set},1,k} \\ i_{\mathrm{set},2,k} \\ \cdots \\ i_{\mathrm{set},M,k} \end{pmatrix}. \tag{21}$$

The $\mathbf{B}$-matrix elements are given as follows:

$$b_{ij} = -\frac{K_{\mathrm{P},j} \cdot N_i N_j V_j}{L_{ij}} \tag{22a}$$

$$b_{ii} = \sum_{m=1}^{M} \frac{K_{\mathrm{P},i} \cdot N_i N_m V_m}{L_{im}}. \tag{22b}$$

The $\mathbf{A}$-matrix elements can be calculated from

$$a_{ij} = \frac{K_{\mathrm{P},j} \cdot N_i N_j V_j}{L_{ij}} \tag{23a}$$

$$a_{ii} = 1 - \sum_{m=1}^{M} \frac{K_{\mathrm{P},i} \cdot N_i N_m V_m}{L_{im}}. \tag{23b}$$

As the magnetization inductance L_{aa} does not pay a role in active power transfer and as assumed in (17) its current $\bar{i}^*_{aa}$ is – assuming no dc bias – ideally 0 at each sampling, we will initially assert

$$L_{aa} = \infty. \tag{24}$$

The effect of dc bias and its mitigation will be discussed in Section III-E.

The dynamics of the system can then be quantified by the eigenvalues λ_i of $\mathbf{A}$. If only stability is concerned, the necessary stability condition must hold

$$|\lambda_i| < 1. \tag{25}$$

When using (23) and (24) to construct $\mathbf{A}$, there will always be at least one λ_i violating (25) by being equal to 1

$$\lambda_1 = 1. \tag{26}$$

This boundary stable eigenvalue indicates a neutral mode state component. In this case, the neutral mode is an equivalence of the sum of energy flow into the transformer. Different from the physical transformer, the description used above allows for the sum of all applied and drawn power not being equal to 0 in a lossless transformer. Therefore, to model the transformer physically correct, the following condition must hold:

$$\sum_{m=1}^{M} \bar{i}^*_{m,k} \cdot V_m \cdot N_m = 0. \tag{27}$$

To bring the model closer to reality, a reduced system $\mathbf{A}_{\mathrm{RS}}$ can be defined, so that the state transitions are still correct, when replacing $\mathbf{A}$ with $\mathbf{A}_{\mathrm{RS}}$

$$\begin{pmatrix} \bar{i}^*_{1,k+1} \\ \bar{i}^*_{2,k+1} \\ \cdots \\ \bar{i}^*_{M,k+1} \end{pmatrix} = \mathbf{A}_{\mathrm{RS}} \begin{pmatrix} \bar{i}^*_{1,k} \\ \bar{i}^*_{2,k} \\ \cdots \\ \bar{i}^*_{M,k} \end{pmatrix} + \mathbf{B} \begin{pmatrix} i_{\mathrm{set},1,k} \\ i_{\mathrm{set},2,k} \\ \cdots \\ i_{\mathrm{set},M,k} \end{pmatrix}. \tag{28}$$

Aside from the last row, the $\mathbf{A}_{\mathrm{RS}}$-matrix elements are still defined the same way as for the $\mathbf{A}$

$$a_{\mathrm{RS},ij} = a_{ij}. \tag{29}$$

To obtain physical accuracy, Eq. (27) can be used to describe the current in the last cell M

$$\bar{i}^*_{M,k} \cdot N_M \cdot V_M = -\sum_{m=1}^{M-1} \bar{i}^*_{m,k} \cdot N_m \cdot V_m. \tag{30}$$

The state progression from $\bar{i}^*_{M,k}$ to $\bar{i}^*_{M,k+1}$ therefore needs to be adjusted. The $\mathbf{A}_{\mathrm{RS}}$-matrix elements of the last row $a_{\mathrm{RS},Mj}$ can be calculated from the sum of all other elements in the same column

$$a_{\mathrm{RS},Mj} = -\sum_{m=1}^{M-1} a_{mj}. \tag{31}$$

For an $M \times M$ $\mathbf{A}_{\mathrm{RS}}$, the Mth row is therefore given as follows:

$$a_{\mathrm{RS},Mj} = -\frac{N_j V_j}{N_M V_M} + \frac{K_{\mathrm{P},j} \cdot N_M N_j V_j}{L_{Mj}} \tag{32a}$$

$$a_{\mathrm{RS},MM} = -\sum_{m=1}^{M} \frac{K_{\mathrm{P},M} \cdot N_M N_m V_m}{L_{Mm}}. \tag{32b}$$

Since this reduces the degree of freedom by 1, there will always be an eigenvalue $\lambda_{\mathrm{RS},1}$ of $\mathbf{A}_{\mathrm{RS}}$ in vanishing mode

$$\lambda_{\mathrm{RS},1} = 0. \tag{33}$$

The asymmetry in currents will accordingly vanish in a single cycle. For stability analysis, the relevant eigenvalues of $\mathbf{A}$ and $\mathbf{A}_{\mathrm{RS}}$ are identical. Only for steady state analysis, as discussed in Section III-F, the difference in the first eigenvalue becomes relevant. Accordingly, a deeper discussion can be found there.

If individual cells operate as constant current loads, their controllers integrator behavior can be modeled just as easily by including an integrated error ε_{I} which propagates as follows:

$$\varepsilon_{\mathrm{I}a,k+1} = \varepsilon_{\mathrm{I}a,k} + (i_{\mathrm{set},a,k} - \bar{i}^*_{a,k}). \tag{34}$$

$\varepsilon_{\mathrm{I}a,k}$ therefore behaves like an additional state. Weighted with an integrator gain $K_{\mathrm{I},a}$, its effect on $\Delta t_{a,k}$ can be included into the control equation

$$\Delta t_{a,k} = -K_{\mathrm{P},a} \cdot (i_{\mathrm{set},a,k} - \bar{i}^*_{a,k}) - K_{\mathrm{I},a} \cdot \varepsilon_{\mathrm{I}a,k}. \tag{35}$$

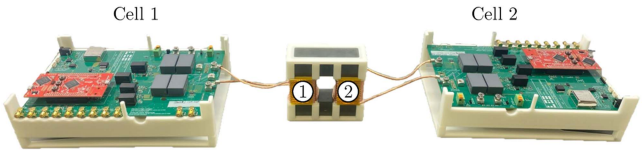

Fig. 13. Two MACs forming a DAB. Each MAC is connected to the shared transformer and controlled by its own MCU (red board).

In general, $\mathbf{A}$ and $\mathbf{B}$ can now be extended to include all ε_{I}, with $K_{\mathrm{I},a}$ being set to 0, if the integrator is not in effect

$$\begin{pmatrix} \bar{i}^*_{1,k+1} \\ \cdots \\ \bar{i}^*_{M,k+1} \\ \varepsilon_{\mathrm{I}1,k+1} \\ \cdots \\ \varepsilon_{M,k+1} \end{pmatrix} = \mathbf{A} \begin{pmatrix} \bar{i}^*_{1,k} \\ \cdots \\ \bar{i}^*_{M,k} \\ \varepsilon_{\mathrm{I}1,k} \\ \cdots \\ \varepsilon_{M,k} \end{pmatrix} + \mathbf{B} \begin{pmatrix} i_{\mathrm{set},1,k} \\ i_{\mathrm{set},2,k} \\ \cdots \\ i_{\mathrm{set},M,k} \end{pmatrix}. \tag{36}$$

For an M cell transformer, $\mathbf{A}$ will be a $2M \times 2M$ and $\mathbf{B}$ a $2M \times M$ matrix. For sake of simplicity, the integrator states will be omitted in the following sections.

B. Example: Stability-Analysis of a DAB

To test the approach in practice, the MAC control is implemented on two cells forming a DAB as shown in Fig. 13. It is important to note, that the full control scheme used to generate the results in this subsection will be explained later in Section III-E. The results shown in this section should therefore be seen as qualitative examples. A full comparison of model and measurement is shown in Section IV-A.

For the DAB, only a single coupling inductance L_{12} as well as the transformation ratio N_2 must to be considered for the transformer model. For the in-lab example, L_{12} was determined to be 63 μH with $N_2 \approx 1$. Each cells input voltages V_1 and V_2 were set to 30 V. Both cells are controlled with their own MCUs without data connection between them. The cell controllers are configured with only a proportional component $K_{\mathrm{P},1}$ and $K_{\mathrm{P},2}$. The $\mathbf{A}$ matrix is therefore given as follows:

$$\mathbf{A} = \begin{pmatrix} 1 - \frac{K_{\mathrm{P},1} \cdot N_2 V_2}{L_{12}} & \frac{K_{\mathrm{P},2} \cdot N_2 V_2}{L_{12}} \\ \frac{K_{\mathrm{P},1} \cdot N_2 V_1}{L_{12}} & 1 - \frac{K_{\mathrm{P},2} \cdot N_2 V_1}{L_{12}} \end{pmatrix}. \tag{37}$$

Solving for the eigenvalues λ leads to

$$\lambda_1 = 1 \tag{38a}$$

$$\lambda_2 = 1 - \frac{K_1 \cdot N_2 V_2 + K_2 \cdot N_2 V_1}{L_{12}}. \tag{38b}$$

As mentioned before, λ_1 is boundary stable, but not physically relevant for the system. For λ_2 to remain stable, the following inequality must hold:

$$0 < \frac{K_1 \cdot N_2 V_2 + K_2 \cdot N_1 V_1}{L_{12}} < 2. \tag{39}$$

TABLE I
STEP RESPONSE COMPARISON: SETTING $i_{\mathrm{SET},1}$ TO 1 A AND $K_{\mathrm{P},1}$ EQUAL TO $K_{\mathrm{P},2}$ SIMULTANEOUSLY RESULTING IN DIFFERENTLY DAMPED SYSTEMS

$K_{\mathrm{P},1}$ in ns/A	$K_{\mathrm{P},2}$ in ns/A	λ_2	State	Fig.
$0 \rightarrow 466$	466	0.6	overdamped	14
$0 \rightarrow 1166$	1166	0	critically damped	15
$0 \rightarrow 1866$	1866	−0.6	underdamped	16
$0 \rightarrow 2799$	2799	−1.2	unstable	17

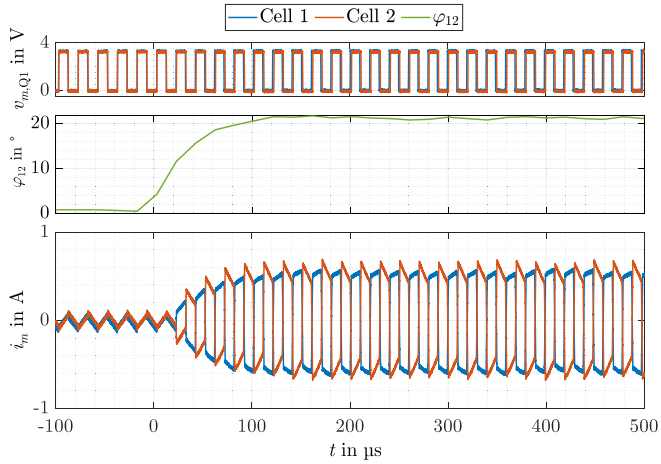

Fig. 14. Experimental measurement results for $\lambda_2 = 0.6$ on a step response of 0.5A.

If the reduced state equations are used, $\mathbf{A}_{\mathrm{RS}}$ is written as follows:

$$\mathbf{A}_{\mathrm{RS}} = \begin{pmatrix} 1 - \frac{K_1 \cdot N_2 V_2}{L_{12}} & \frac{K_2 \cdot N_2 V_2}{L_{12}} \\ -\frac{V_1}{N_2 V_2} + \frac{K_1 \cdot N_2 V_1}{L_{12}} & -\frac{K_2 \cdot N_2 V_1}{L_{12}} \end{pmatrix}. \tag{40}$$

In this case, λ_{RS} is given as follows:

$$\lambda_{\mathrm{RS},1} = 0 \tag{41a}$$

$$\lambda_{\mathrm{RS},2} = 1 - \frac{K_1 \cdot N_2 V_2 + K_2 \cdot N_2 V_1}{L_{12}}. \tag{41b}$$

As intended, $\lambda_{\mathrm{RS},1}$ is 0 and the eigenvalues λ_2 and $\lambda_{\mathrm{RS},2}$ are equal.

To investigate the system, $K_{\mathrm{P},1}$ and $K_{\mathrm{P},2}$ were adjusted to result in different λ_2 of 0.6, 0, −0.6 and −1.2 while applying a fixed step response of 0.5A. To obtain a stable initial OP, $K_{\mathrm{P},2}$ was set to a fixed stable value and $K_{\mathrm{P},1}$, $i_{\mathrm{set},1}$, and $i_{\mathrm{set},2}$ were set to 0. The step response was then triggered through setting $i_{\mathrm{set},1}$ to 1A and $K_{\mathrm{P},1}$ equal to $K_{\mathrm{P},2}$ simultaneously. This allows for the same OP current i_{OP} of ±0.5 A for each measurement, while also being able to change from stable to unstable OP in the case of $\lambda_2 = -1.2$. The parameters for the step response comparison are summarized in Table I.

The step response for λ_2 of 0.6 is shown in Fig. 14. As expected, the MMAB finds a stable OP of ±0.5 A. As λ_2 is greater than 0, the OP is reached monotonously without oscillation. The phase shift φ_{12} therefore takes multiple cycles to increase to its final value.

In Fig. 15, $K_{\mathrm{P},1}$ and $K_{\mathrm{P},2}$ were selected to realize a λ_2 of 0. The OP is now reached after a single switching period T. In

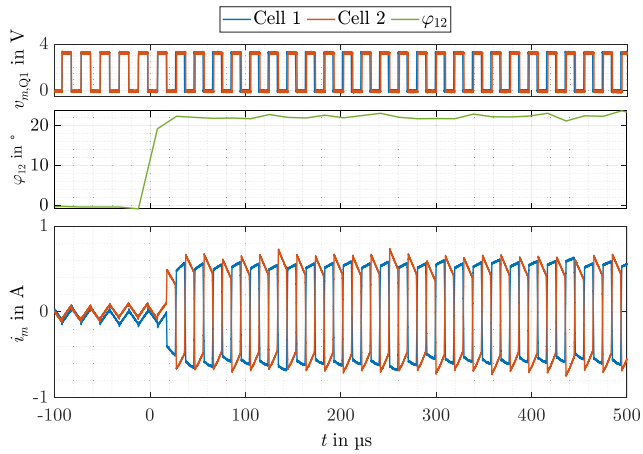

Fig. 15. Experimental measurement results for a calculated $\lambda_2 = 0$ on a step response of 0.5A.

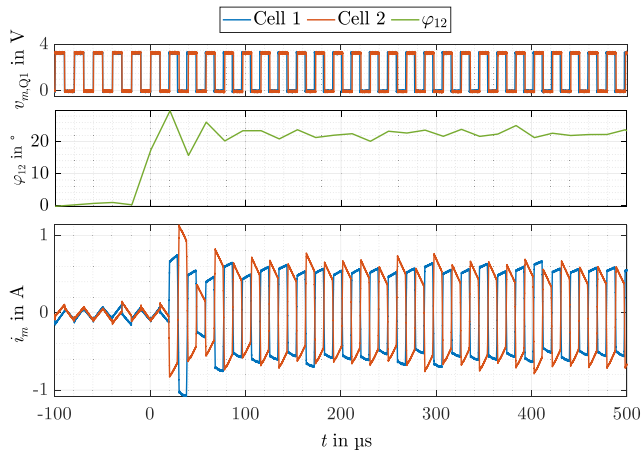

Fig. 16. Experimental measurement results for $\lambda_2 = -0.6$ on a step response of 0.5A. The current shows overshoot due to the negative eigenvalue.

terms of dynamics, this can be seen as optimal MAC control. In terms of susceptibility to noise, higher dynamics will lead to more oscillations during normal operation. In terms of phase shift, it can be observed that K_P has no impact on the steady-state value.

Increasing $K_{\mathrm{P},1}$ and $K_{\mathrm{P},2}$ further leads to a negative λ_2. The resulting step response for $\lambda_2 = -0.6$ is shown in Fig. 16. As expected, the step response now leads to overshoot. Still, the MMAB will find a stable OP. In practice, λ below 0 are not advised

Once $\lambda_2 < -1$, the system becomes unstable. In Fig. 17, λ_2 is increased from -0.1 to -1.2. The MMAB therefore no longer maintains a stable OP. According to the model, the currents would oscillate with increasing amplitude. As the state equations are accurate only for absolute phase shifts below $\pi/2$, the model cannot accurately describe the physical system anymore. For larger absolute phase shifts, the MMAB enters triangular mode, which will be explained in the next section. Instead of ever increasing amplitude, the MMAB continuously

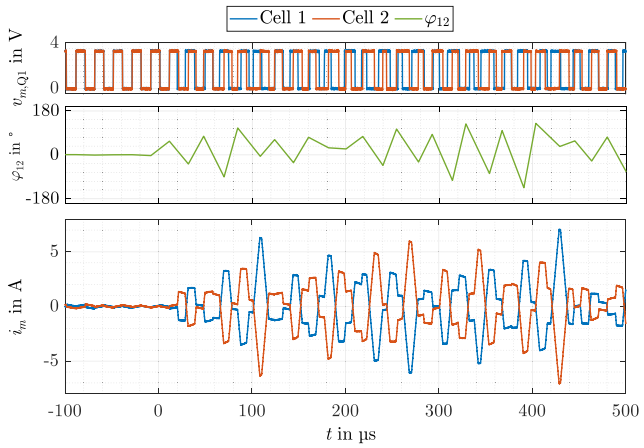

Fig. 17. Experimental measurement results for $\lambda_2 = -1.2$ on a step response of 0.5A from a system with $\lambda_2 = -0.1$. The system oscillates unstably after the step response.

shifts between trapezoidal and triangular modes in a nonlinear oscillation pattern.

Aside from describing the effects different eigenvalues have on the system, the findings also show the consequence of parameter mismatch. As given in (41), the eigenvalues depend on the control parameters, the cell voltages, and the coupling inductance. Instabilities due to control parameter mismatch are caused when the eigenvalue crosses -1. Assuming one set of control parameters for the whole operating range, the most critical point occurs at maximum cell voltages and the lowest inductance. While the maximum cell voltages should be known for any application, the coupling inductance may be misestimated during the design process, or shift in value due to core-temperature. As long as the expected eigenvalues stay positive, even larger variations in coupling inductance, e.g., L_{12} being halved, will not cause instability. It is still advised to properly characterize the transformer in all operating conditions before setting final control parameters.

C. State-Space Model of Active Currents in Triangular Mode

As observed in the unstable DAB example, the developed model is only accurate while the absolute phase shift of two cells is below $\pi/2$. For higher absolute phase shifts, the two cells enter triangular mode. In triangular mode – using the same sampling point in the center of the positive half-wave as in trapezoidal mode – the state $\bar{i}^*_{ab,k}$ can be written as follows:

$$\bar{i}^*_{ab,k} = \frac{N_a N_b V_b}{L_{ab}} \cdot (-\delta t_k). \tag{42}$$

Compared to the trapezoidal mode [see (18)], the sign of δt_k is flipped. Similarly, the state transition equation also differs only in sign

$$\bar{i}^*_{ab,k+1} = \bar{i}^*_{ab,k} + \frac{N_a N_b V_b}{L_{ab}} \cdot (\Delta t_{a,k} - \Delta t_{b,k}). \tag{43}$$

To integrate the change in sign, an additional viable ζ_{ab} can be added for each port combination a and b. ζ_{ab} changes sign, once

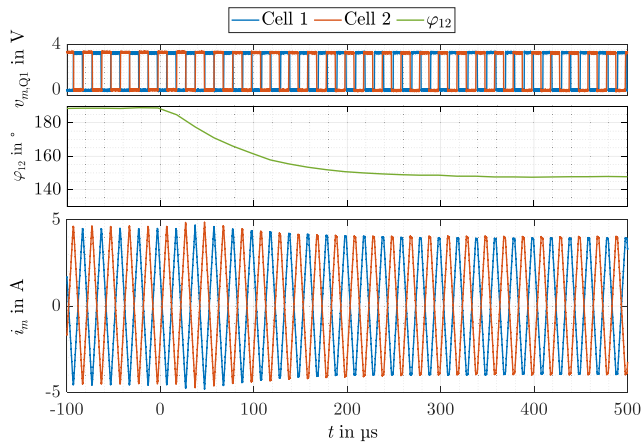

Fig. 18. Experimental measurement results of the operation and step response of two MAC with negative K_P values operating in triangular mode.

the absolute value of φ_{ab} crosses the $\pi/2$ threshold

$$\zeta_{ab} = \mathrm{sign}(\cos(\varphi_{ab})). \tag{44}$$

Different from the linear discrete time system introduced above, the inclusion of ζ_{ab} requires knowledge of the current OP of the system. A method for finding ζ_{ab} will be discussed in Section III-F. For a generalized solution, $\mathbf{A}$ and $\mathbf{B}$ can be adjusted for the possible mode change

$$a_{ij} = \zeta_{ij} \frac{K_j \cdot N_j V_j}{L_{ij}} \tag{45a}$$

$$a_{ii} = 1 - \sum_{m=1}^{M} \zeta_{im} \frac{K_i \cdot N_m V_m}{L_{im}} \tag{45b}$$

$$b_{ij} = -\zeta_{ij} \frac{K_j \cdot N_j V_j}{L_{ij}} \tag{45c}$$

$$b_{ii} = \sum_{m=1}^{M} \zeta_{im} \frac{K_i \cdot N_m V_m}{L_{im}}. \tag{45d}$$

When only considering a DAB, MAC control can be set up to operate only in triangular mode by selecting negative values for $K_{\mathrm{P},1}$ and $K_{\mathrm{P},2}$. As shown in Fig. 18, the control behaves exactly as in trapezoidal mode, albeit with the frequency and, therefore, phase shift decreasing in a positive step response.

In general, the MMAB cannot operate in triangular mode between all cells. Even for three cells connected to one transformer, a phase shift of π between cells 1 and 2 as well as π between 1 and 3 would already lead to a phase shift of 0 between cells 2 and 3. Therefore, a control scheme based only on negative K_P to force triangular mode operation would not be possible in multicell transformers.

In contrast, individual cells of the MMAB entering triangular mode during regular operation is possible. This can occur, if the load current between two cells is increased above a limit. If the system remains stable needs to be investigated depending on the new state transition matrix. The effect will be shown exemplarily in the next section.

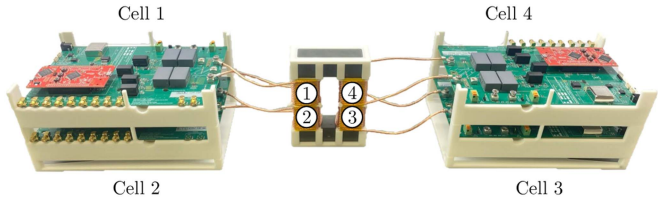

Fig. 19. A total of 4 cells of an MMAB on a shared transformer. Each cell is controlled by its own MCU.

TABLE II
MEASURED INDUCTANCE VALUES, TRANSFORMATION RATIOS, AND COUPLING FACTORS

Variable	Value
L_{11} in µH	670
N_2	1.012
N_3	1.047
N_4	1.047

Variable	Value
L_{12} in µH	39.6
L_{13} in µH	-380.0
L_{14} in µH	90.7
L_{23} in µH	90.4
L_{24} in µH	-391.0
L_{34} in µH	40.1

Variable	Value
k_{12}	0.9743
k_{13}	0.9442
k_{14}	0.9496
k_{23}	0.9504
k_{24}	0.9443
k_{34}	0.9758

D. Example: 4-Port Stability Under Different Phase Angles

To investigate the effect of mode changing, a 4-cell MMAB is tested on a single transformer as shown in Fig. 19. Each cell is still controlled by its own MCU with no data connection between any of the cells. The cells are controlled with proportional controllers with 167 ns/A each and connected to the same 30 V voltage source.

The transformer is modeled with the equivalent circuit shown in Fig. 11, with the measured values given in Table II.

The negative inductance for L_{13} and L_{24} is due to the modeling approach. In practice, every measurable inductance – every inductance that can be measured from any cell a to cell b – is positive, as every negative inductance in the model has smaller positive inductances in parallel. Readers too uncomfortable with negative inductance can use the coupling factors k_{ab} in Table II. The resulting system stays the same. The transformer was not designed for optimal operation for a 4-cell MMAB, but rather to showcase operation between differently coupled cells.

Initially, the set values for all cells are 0 A. The system eigenvalues using $\mathbf{A}_\mathrm{RS}$ are shown as blue circles in Fig. 20. A step response is now applied to the set value of cell 3.

Due to the lowest coupling between cell 1 and cell 3, φ_{13} will be the first phase shift to cross 90°, if the step response is high enough. A −4 A set-value step response at cell 3 is shown in Fig. 21. At 380 μs – indicated by the black dashed line in Fig. 21 – φ_{13} crosses 90° and at that point ζ_{13} becomes negative. $\mathbf{A}_\mathrm{RS}$ is therefore changed and its eigenvalues move as indicated by the red stars in Fig. 20. While the dynamics change, no λ crosses into the unstable region and the system continues to converge towards its OP.

If a −5 A step response is applied, then not only φ_{13} but eventually also φ_{23} will increase over 90°. The eigenvalues for this case are shown in Fig. 20 as yellow crosses. Different from before, the system now exhibits an unstable λ. Unlike the instability in Fig. 17, the unstable λ is now positive, which

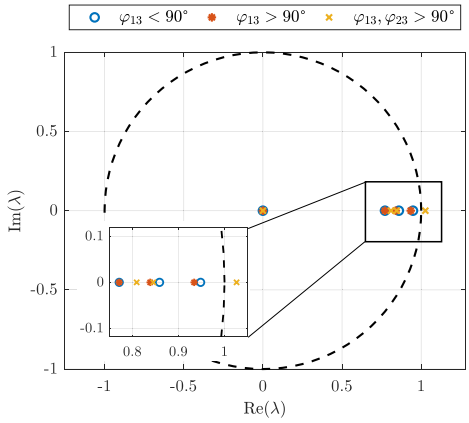

Fig. 20. Eigenvalues of $\mathbf{A}_{\mathrm{RS}}$ under different phase shifts. While φ_{13} greater 90° still leads to a stable system, both φ_{13} and φ_{23} greater 90° leads to a single unstable λ greater 1.

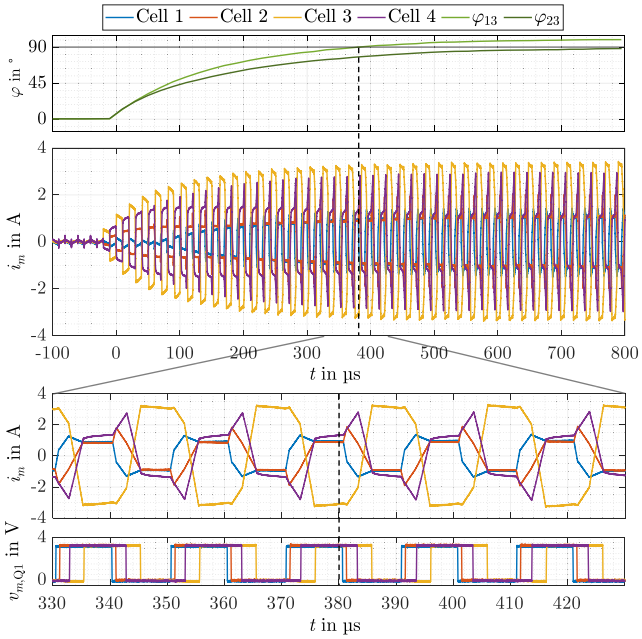

Fig. 21. Experimental measurement results of a step response leading to φ_{13} greater 90°. The MMAB still finds a stable operating point.

indicates a monotonous exponential increase – similar to a single right half plane pole in time continuous systems – instead of oscillating behavior. The effect can be observed in Fig. 22. After φ_{23} increases over 90°, φ_{23} starts to increase exponentially. Similarly, the currents start to become increasingly triangular.

E. State-Space Model and Control Including DC-Bias

Different from resonant converters, the DAB can suffer from involuntary dc-bias [62], [63], [64]. Unlike with fixed frequency DAB control, a step response will not lead to dc-bias in MAC control as introduced so far. Since the positive half-wave $T_{\mathrm{p},k}$ and negative half-wave $T_{\mathrm{n},k}$ will be changed by the same $\delta t_k/2$, a step response should not introduce any dc voltage $\bar{u}_{\mathrm{DC}}$. Still, a residual delay mismatch from the MCU to the transistors can

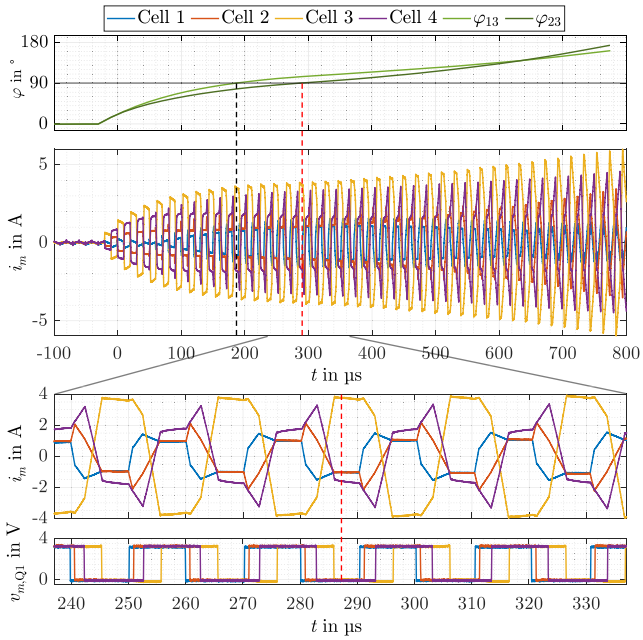

Fig. 22. Experimental measurement results of a step response leading to φ_{23} greater 90° after the red dashed line. The MMAB becomes unstable with φ_{13} and φ_{23} exponentially increasing.

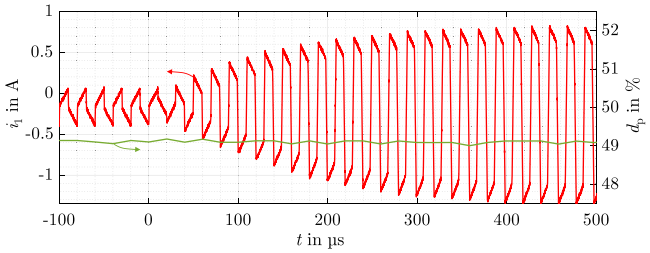

Fig. 23. Experimental measurement results of a step response on a MAC without DC-bias compensation. The DC-bias was artificially increased through the PWM for better visibility. d_{p} is calculated from the measured gate signal $v_{1,\mathrm{Q1}}$.

introduce a residual $\bar{u}_{\mathrm{DC},a}$ on the transformer at any given cell a. $\bar{u}_{\mathrm{DC},a}$ can be defined as follows:

$$\bar{u}_{\mathrm{DC},a} = V_a \cdot (d_{\mathrm{p}} - 0.5). \tag{46}$$

In this case d_{p} is the ratio of the positive half-wave $T_{\mathrm{p},k}$ to the whole switching period T:

$$d_{\mathrm{p}} = \frac{T_{\mathrm{p},k}}{T}. \tag{47}$$

Assuming $\bar{u}_{\mathrm{DC},a}$ to be constant and given an effective dc resistance R_{DC} for cell a, the long term dc current $\bar{i}_{\mathrm{DC},a}$ into the transformer will be

$$\bar{i}_{\mathrm{DC},a} = \frac{V_a}{R_{\mathrm{DC}}} \cdot (d_{\mathrm{p}} - 0.5). \tag{48}$$

The effect is shown in Fig. 23 for an artificially reduced d_{p}. It is important to note that d_{p} needs to be calculated at the switching node and not at the output of the MCU, as for example delay mismatches within gate drivers, or even current or voltage dependent

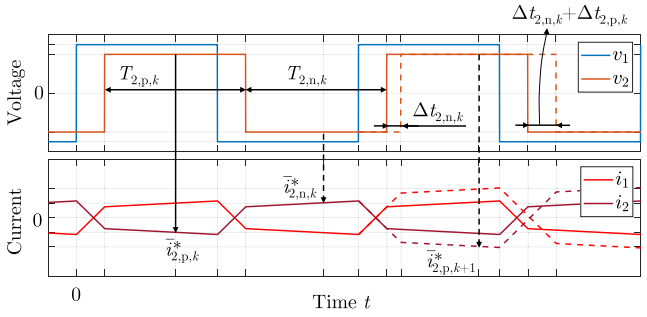

Fig. 24. Fundamental waveforms of a two cell MMAB with control of both positive and negative half-waves. The sampling in cell 2 is indicated by the vertical black arrows. The length of the negative half-wave is adjusted by $\Delta t_{2,n,k}$, the length of the positive by $\Delta t_{2,p,k}$.

differences in rise and fall times of the transistors drain-source voltages can have an effect on d_p. Furthermore, unlike with regular DAB control, a step response on the frequency variable control scheme discussed in the previous sections has no direct impact on d_p.

As this dc bias can lead to increased losses or even complete saturation of the transformer, dc blocking capacitors might be required. Albeit, as these introduce additional losses, volume, and costs, active dc bias compensation would be preferable.

The MAC control can achieve active dc bias compensation, if $\bar{i}^*_a$ is sampled once every half period. The principle is shown in Fig. 24. By sampling in the positive and negative half-wave, $\bar{i}^*_{a,k}$ becomes two states. $\bar{i}^*_{a,\mathrm{p},k}$ and $\bar{i}^*_{a,\mathrm{n},k}$ now represent the sampled current in the positive and negative half-wave. These can now be used to change the length of the half-waves $T_{a,\mathrm{p},k}$ and $T_{a,\mathrm{n},k}$ independently by the control signals $\Delta t_{a,\mathrm{p},k}$ and $\Delta t_{a,\mathrm{n},k}$

$$T_{a,\mathrm{p},k} = \frac{T}{2} + \Delta t_{a,\mathrm{p},k} \tag{49}$$

$$T_{a,\mathrm{n},k} = \frac{T}{2} + \Delta t_{a,\mathrm{n},k}. \tag{50}$$

For the stability of the control, it is required that $\Delta t_{a,\mathrm{p},k}$ is controlled by $\bar{i}^*_{a,\mathrm{n},k}$ and $\Delta t_{a,\mathrm{n},k}$ by $\bar{i}^*_{a,\mathrm{p},k}$. This can best be explained by only accounting for the part of the measured current $\bar{i}^*_{aa}$ coming from the magnetization inductance L_{aa}. Using just a single sampling per switching period, the state transition can be described as follows:

$$\bar{i}^*_{aa,k+1} = \bar{i}^*_{aa,k} + \frac{V_a}{L_{aa}} \cdot T_{a,\mathrm{p},k} - \frac{V_a}{L_{aa}} \cdot T_{a,\mathrm{n},k}. \tag{51}$$

Here, L_{aa} is the magnetization inductance as seen from cell a. When using the ECM from Fig. 11, only L_{11} is directly given, with all other L_{aa} needed to be calculated from N_a and the series–parallel connection of all stray inductances in the transformer. By sampling once per half-wave, $\bar{i}^*_{aa}$ will now be measured as a magnetization component in the positive half-wave $\bar{i}^*_{aa,\mathrm{p},k}$ and a magnetization component in the negative half-wave $\bar{i}^*_{aa,\mathrm{n},k}$. Both are interlinked by

$$\bar{i}^*_{aa,\mathrm{p},k} = -\bar{i}^*_{aa,\mathrm{n},k}. \tag{52}$$

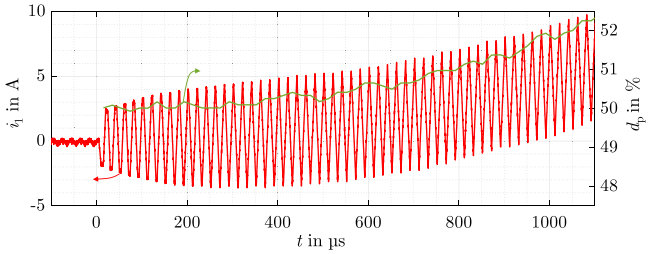

Fig. 25. Experimental measurement results after the turn on of a MAC where the length of a half-wave is controlled by the current of same signage. The system is unstable and the DC-bias exponentially increases.

In practice, both positive and negative current will be controlled identically. To keep equations consistent with previous sections, we set both controllers K_Pp and K_Pn for both $\bar{i}^*_{a,\mathrm{p},k}$ and $\bar{i}^*_{a,\mathrm{n},k}$ as follows:

$$K_\mathrm{Pp} = -K_\mathrm{Pn} = \frac{K_\mathrm{P}}{2}. \tag{53}$$

This way K_P can be used in all equations, leading to the same results as previous sections. $\Delta t_{a,\mathrm{p},k}$ and $\Delta t_{a,\mathrm{n},k}$, therefore, share the same relation

$$\Delta t_{a,\mathrm{p},k} = -\Delta t_{a,\mathrm{n},k}. \tag{54}$$

This fact is independent of the control relationship between positive and negative half-wave measurement and control. If we assume $\bar{i}^*_{aa,\mathrm{p},k}$ to control $\Delta t_{a,\mathrm{p},k}$, then

$$\Delta t_{a,\mathrm{p},k} = \frac{K_\mathrm{P}}{2} \cdot \bar{i}^*_{aa,\mathrm{p},k}. \tag{55}$$

The state propagation of $\bar{i}^*_{aa,\mathrm{p},k}$ is therefore given as follows:

$$\bar{i}^*_{aa,\mathrm{p},k+1} = \left(1 + K_\mathrm{P} \frac{V_a}{L_{aa}}\right) \cdot \bar{i}^*_{aa,\mathrm{p},k}. \tag{56}$$

As can be directly seen, (56) diverges and therefore indicates an unstable system.[1] The effect can be seen in Fig. 25 for a DAB. In this case Cell 2 was operating stably at no load, with Cell 1 being turned ON. As the dc bias of Cell 1 is controlled according to (56), d_p increases exponentially leading to a quickly increasing dc bias. As mentioned, the correct control law needs to be

$$\Delta t_{a,\mathrm{p},k} = \frac{K_\mathrm{P}}{2} \cdot \bar{i}^*_{aa,\mathrm{n},k}. \tag{57}$$

This will therefore lead to a stable and converging system, assuming K_P to be sufficiently low

$$\bar{i}^*_{aa,\mathrm{p},k+1} = \left(1 - K_\mathrm{P} \frac{V_a}{L_{aa}}\right) \bar{i}^*_{aa,\mathrm{p},k}. \tag{58}$$

The effect of dc bias compensation is shown in Fig. 26. Here, d_p is continuously readjusted to eliminate dc bias. The effect is intrinsic, since $\bar{i}^*_{aa,\mathrm{p},k}$ and $\bar{i}^*_{aa,\mathrm{n},k}$ are controlled to be the same absolute value.

[1] An attentive reader might notice, that when a DAB is supposed to operate in triangular mode, i.e., with negative K_P values, then the length of the half-waves must be controlled by the current with same sinage.

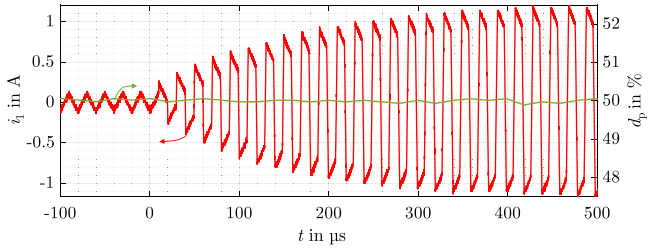

Fig. 26. Experimental measurement results of a single MAC under proper control of positive and negative half-waves. DC-bias compensation is system imminent under this control scheme.

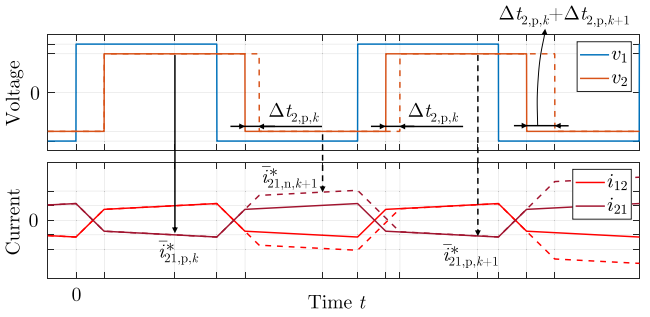

Fig. 27. Example of the reaction of the sampled currents $\bar{i}^*_{21,n}$ and $\bar{i}^*_{21,p}$, when only the positive half-wave pulse-width is increased.

The division in negative and positive parts can also be represented in the state-space model by doubling the number of state variables

$$\begin{pmatrix} \bar{i}^*_{1,p,k+1} \\ \cdots \\ \bar{i}^*_{M,p,k+1} \\ \cdots \\ \varepsilon_{M,p,k+1} \\ \bar{i}^*_{1,n,k+1} \\ \cdots \\ \bar{i}^*_{M,n,k+1} \\ \cdots \\ \varepsilon_{M,n,k+1} \end{pmatrix} = \mathbf{A}_{PN} \begin{pmatrix} \bar{i}^*_{1,p,k} \\ \cdots \\ \bar{i}^*_{M,p,k} \\ \cdots \\ \varepsilon_{M,p,k} \\ \bar{i}^*_{1,n,k} \\ \cdots \\ \bar{i}^*_{M,n,k} \\ \cdots \\ \varepsilon_{M,n,k} \end{pmatrix} + \mathbf{B}_{PN} \begin{pmatrix} i_{set,1,p,k} \\ \cdots \\ i_{set,M,p,k} \\ i_{set,1,n,k} \\ \cdots \\ i_{set,M,n,k} \end{pmatrix}. \quad (59)$$

Unlike with the magnetization inductance L_{aa}, a change in $\Delta t_{a,p,k}$ affects only the negative current $\bar{i}^*_{a,n,k+1}$. This can be explained by applying a $\Delta t_{2,p,k}$ to the active current $\bar{i}^*_{21}$ shown in Fig. 27. We first assume the two ports 1 and 2 to be in steady state with no dc bias.

$$\bar{i}^*_{21,p,k} = -\bar{i}^*_{21,n,k} \quad (60)$$

While the change $\Delta\bar{i}^*_{21}$ can be seen in $\bar{i}^*_{21,n,k+1}$.

$$\bar{i}^*_{21,n,k+1} = \bar{i}^*_{21,n,k} + \frac{\Delta t_{2,p,k} \cdot N_1 V_1}{L_{12}}. \quad (61)$$

The next $\bar{i}^*_{21,p,k+1}$ will be unaffected, since

$$\bar{i}^*_{21,p,k+1} = -\bar{i}^*_{21,n,k+1} - \frac{\Delta t_{2,p,k} \cdot N_1 V_1}{L_{12}} = \bar{i}^*_{21,p,k}. \quad (62)$$

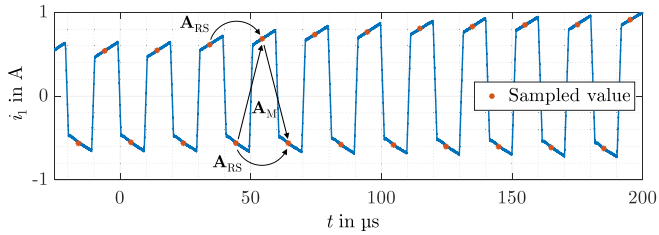

Fig. 28. Experimental waveforms of the current step response on the change of only the positive current component. $\mathbf{A}_{RS}$ affects the progression from positive to positive half-wave, as well as negative to negative half-wave, while $\mathbf{A}_M$ couples positive and negative currents.

Only for the magnetization inductance L_{aa}, the change in d_p, as explained above, will show an effect. For an M-cell MMAB, the $\mathbf{A}_{PN}$ matrix can be defined by four sub-matrices

$$\mathbf{A}_{PN} = \begin{pmatrix} \mathbf{A}_{RS} & \mathbf{A}_M \\ \mathbf{A}_M & \mathbf{A}_{RS} \end{pmatrix}. \quad (63)$$

The sub-matrices on the diagonals are identical to $\mathbf{A}_{RS}$, under the condition that the integral and proportional gains are halved according to (53) when $\bar{i}^*_p$ and $\bar{i}^*_n$ are controlled individually. Otherwise the equations (45) need to be adjusted with a factor of 2 at each K. The magnetization matrices $\mathbf{A}_M$ describe the effect of L_{aa} on the system. They can be constructed as diagonal matrices

$$a_{ii} = \frac{K_{P,i} \cdot N_i V_i}{L_{ii}} \quad (64a)$$

$$a_{ij} = 0. \quad (64b)$$

Additional states for integrators can be added as described in Section III-A. The effect of $\mathbf{A}_{RS}$ and $\mathbf{A}_M$ within $\mathbf{A}_{PN}$ can be best explained with a step response of only the positive current set-value $i_{set,1,p,k}$ as shown in Fig. 28. $\mathbf{A}_{RS}$ in this case represents the effect $\bar{i}^*_{1,p,k}$ has on the next step $\bar{i}^*_{1,p,k+1}$. $\mathbf{A}_M$ on the other hand, represents the coupling between $\bar{i}^*_{1,p,k}$ and $\bar{i}^*_{1,n,k+1}$. Since L_{11} is typically much higher than L_{12}, the effect of a $i_{set,1,p}$ step change on $\bar{i}^*_{1,p,k+1}$ is much more pronounced than on $\bar{i}^*_{1,n,k+1}$.

This effect can become especially pronounced, if cells only control either the positive or negative half-wave current component. If all windings are oriented the same way, one component would suffice. If instead – due to manufacturing benefits – some windings are flipped by 180 °, some cells would control $\bar{i}^*_{p,k}$, whereas some cells would control $\bar{i}^*_{n,k}$. The resulting response would in this case resemble the waveform depicted in Fig. 28. Due to this effect, it is strongly recommended to control both positive and negative components, if no dc-blocking capacitors are used.

While the state-space model doubles, the eigenvalues of $\mathbf{A}_{PN}$ share a specific relationship with the eigenvalues of $\mathbf{A}_{RS}$. As the order is doubled, each λ_i of $\mathbf{A}_{RS}$ has two corresponding eigenvalues λ_{ia} and λ_{ib} of $\mathbf{A}_{PN}$. If L_{aa} is set infinitely large, $\mathbf{A}_{PN}$ is a block diagonal matrix and its eigenvalues – albeit doubled

– are equal to the eigenvalues of $\mathbf{A}_{\mathrm{RS}}$

$$\lambda_{i,a} = \lambda_{i,b} = \lambda_{\mathrm{RS},i}. \tag{65}$$

In many cases, the eigenvalues $\lambda_{i,a/b}$ can be assumed close to $\lambda_{\mathrm{RS},i}$, as L_{aa} is typically large compared to L_{ab}. For stability analysis it is therefore possible to use the lower order $\mathbf{A}_{\mathrm{RS}}$, if all $\lambda_{\mathrm{RS},i}$ are set > 0 as advised. Albeit, if coupling factors become too low, the change in eigenvalues can start negatively effecting the stability of the system.

In terms of linking the state model to real continuous-time propagation, it is important to note that $\bar{i}^*_{a,\mathrm{p},k}$ and $\bar{i}^*_{a,\mathrm{n},k}$ propagate simultaneously, but actually occur successively. Especially regarding reaction to set value changes, this requires $i_{\mathrm{set},a,\mathrm{p},k}$ and $i_{\mathrm{set},a,\mathrm{p},k}$ to change at the same time in reality, to be representable by the model.

F. Operating Point

Since application oriented design requires information about phase-shifts and operating frequencies, steady state operating points need to be calculated. In this section, the steady-state values will be computed and are represented by capitalized letters for distinction from the dynamic state variables. The system achieves steady-state when the subsequent equality is satisfied

$$\begin{pmatrix} \bar{I}^*_1 \\ \dots \\ \bar{I}^*_M \\ E_{\mathrm{I}1} \\ \dots \\ E_M \end{pmatrix} \overset{!}{=} \mathbf{A}_{\mathrm{RS}} \begin{pmatrix} \bar{I}^*_1 \\ \dots \\ \bar{I}^*_M \\ E_{\mathrm{I}1} \\ \dots \\ E_M \end{pmatrix} + \mathbf{B} \begin{pmatrix} I_{\mathrm{set},1} \\ I_{\mathrm{set},2} \\ \dots \\ I_{\mathrm{set},M} \end{pmatrix}. \tag{66}$$

E_{I} are the steady state values of the integrator errors $\varepsilon_{\mathrm{I}1}$. By reordering (66), the solution can be directly found

$$\begin{pmatrix} \bar{I}^*_1 \\ \dots \\ \bar{I}^*_M \\ E_{\mathrm{I}1} \\ \dots \\ E_M \end{pmatrix} = (\mathbf{I} - \mathbf{A}_{\mathrm{RS}})^{-1}\mathbf{B} \begin{pmatrix} I_{\mathrm{set},1} \\ I_{\mathrm{set},2} \\ \dots \\ I_{\mathrm{set},M} \end{pmatrix}. \tag{67}$$

This approach is only possible, if $\mathbf{A}_{\mathrm{RS}}$ is used since

$$(\mathbf{I} - \mathbf{A})^{-1}\mathbf{B} = \mathbf{I}. \tag{68}$$

$\mathbf{A}$ can therefore not give a sensible solution for the OP.

From the steady state currents, the switching frequency F_{s} can be calculated. In steady-state, F_{s} must be equal in all cells, since (13) is valid regardless of whether all $K_{\mathrm{I},m}$ are 0 or not. The ΔT_a by which the unperturbed switching period T_0 is adjusted can be determined by the stead-state control control law derived from (35)

$$\Delta T_a = -K_{\mathrm{P},a} \cdot (I_{\mathrm{set},a} - \bar{I}^*_a) - K_{\mathrm{I},a} \cdot E_{\mathrm{I}a}. \tag{69}$$

F_{s} can therefore be calculated from the steady state switching period T_{s}

$$\frac{1}{F_{\mathrm{s}}} = T_{\mathrm{s}} = T_0 + \Delta T_a. \tag{70}$$

To calculate the ζ values, the phase shifts φ_{ab} are required. To obtain these, the partial currents $\bar{I}^*_{ab}$ can be related to the time lags/leads δT_{ab}

$$\bar{I}^*_{ab} = \frac{N_1 N_2 V_2}{L_{12}} \delta T_{ab}. \tag{71}$$

As there are only $M-1$ linear independent phase shifts of M-cells, each δT_{ab} is referenced to the last cell M

$$\delta T_{ab} = \delta T_{aM} - \delta T_{bM}. \tag{72}$$

The currents $\bar{I}^*_a$ can therefore expressed in relation to the individual δT_{aM} through the matrix $\mathbf{P}$

$$\begin{pmatrix} \bar{I}^*_1 \\ \dots \\ \bar{I}^*_{M-1} \end{pmatrix} = \mathbf{P} \begin{pmatrix} \delta T_{1M} \\ \dots \\ \delta T_{(M-1)M} \end{pmatrix}. \tag{73}$$

Due to the reference to phase M, $\mathbf{P}$ is a $M-1 \times M-1$ matrix, with the entries p_{ab} given as

$$p_{ii} = -\frac{N_i N_i V_i}{L_{ii}} + \sum_{m=1}^{M} \zeta_{im} \frac{N_i N_m V_m}{L_{im}} \tag{74a}$$

$$p_{ij} = -\zeta_{ij} \frac{N_i N_j V_j}{L_{ij}}. \tag{74b}$$

The first term in (74) is added to account for the fact that L_{ii} does not participate in active power transfer. By inversion of $\mathbf{P}$, the steady state δT_{aM} can be directly calculated

$$\begin{pmatrix} \delta T_{1M} \\ \dots \\ \delta T_{(M-1)M} \end{pmatrix} = \mathbf{P}^{-1} \begin{pmatrix} \bar{I}^*_1 \\ \dots \\ \bar{I}^*_{M-1} \end{pmatrix} \tag{75}$$

Finally, φ_{ab} can be determined from δT_{ab}

$$\varphi_{ab} = 2\pi \frac{\delta T_{ab}}{T_{\mathrm{s}}}. \tag{76}$$

If any φ_{ab} is larger than $\pi/2$, ζ_{ab} must be adjusted accordingly and all calculations repeated. As this change affects each step before, this procedure should be repeated until each ζ_{ab} is as expected

IV. Model Verification

A. MAC-Model Verification on a DAB

To verify the full modeling approach, the DAB in Fig. 13 is investigated under MAC control of positive and negative half-waves. L_{12} was measured to be 63 μH and L_{11} 930 μH, voltages at both cells were set 30 V with $N_2 \approx 1$ and K_{P} was selected as 467 ns/A. The eigenvalues of the system are plotted in Fig. 29 and given in Table III. As expected, the eigenvalues of $\mathbf{A}_{\mathrm{PN}}$ are equal to $\mathbf{A}_{\mathrm{RS}}$ for an infinitely large L_{11} and L_{22}. If the

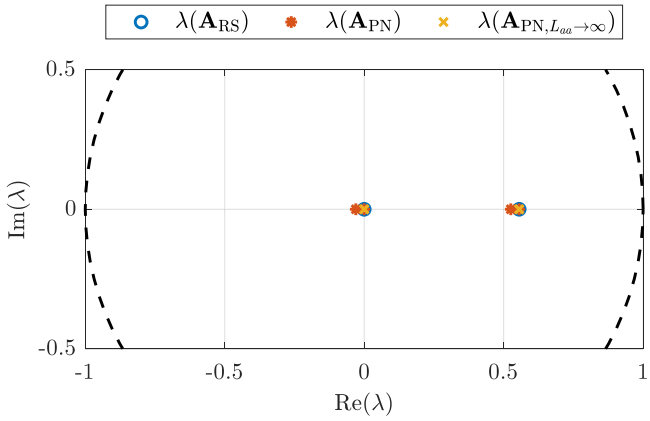

Fig. 29. Eigenvalues of the system calculated with different $\mathbf{A}$-matrices.

TABLE III
EIGENVALUES OF THE SYSTEM CALCULATED WITH DIFFERENT $\mathbf{A}$-MATRICES

λ	$\mathbf{A}_{\mathrm{RS}}$	$\mathbf{A}_{\mathrm{PN}}$	$\mathbf{A}_{\mathrm{PN},L_{aa}\to\infty}$
λ_1	0	0	0
λ_2	0.56	0.56	0.56
λ_3	-	–0.03	0
λ_4	-	0.53	0.56

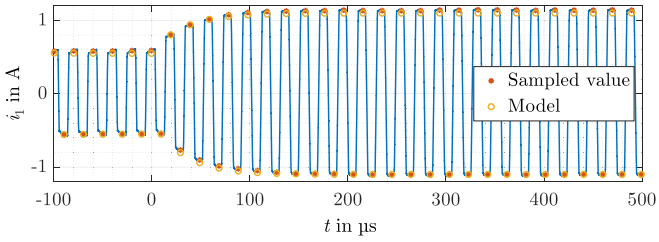

Fig. 30. Comparison of model (yellow circles) and measurement. The measured currents at the sampling instances are indicated as red stars.

magnetization inductances are included, the eigenvalues shift only slightly with the eigenvalues of $\mathbf{A}_{\mathrm{RS}}$ still being included.[2]

To validate the model, a step response from a set value of 1 to 2 A on cell 1 was applied to the system as shown in Fig. 30. The step was not applied from 0, as it was observed that $\Delta t_{1,\mathrm{n/p},k}$ could be affected by the half-bridges dead-time. In this case, a large signal step response would lead to the parasitic capacitances being discharged more quickly for the second half-wave, leading to a disconnect between model and measurement. The effect can be seen in Figs. 14–17, where the negative half-wave absolute value is different from the positive half-wave right after the step response. We therefore additionally reduced dead times to 25 ns, to minimize the effect. Aside from a slight dc-offset, model (yellow circles) and and the sampled measurement (red stars) in Fig. 30 match almost perfectly. We attribute the offset to calibration mismatches within the cells

[2] Interestingly, λ_3 and λ_4 are equal to the eigenvalues of $\mathbf{A}_{\mathrm{RS}}$ minus the eigenvalues of $\mathbf{A}_{\mathrm{M}}$. In preparation of this work, we were not able to find a mathematical proof showing that this relationship must hold.

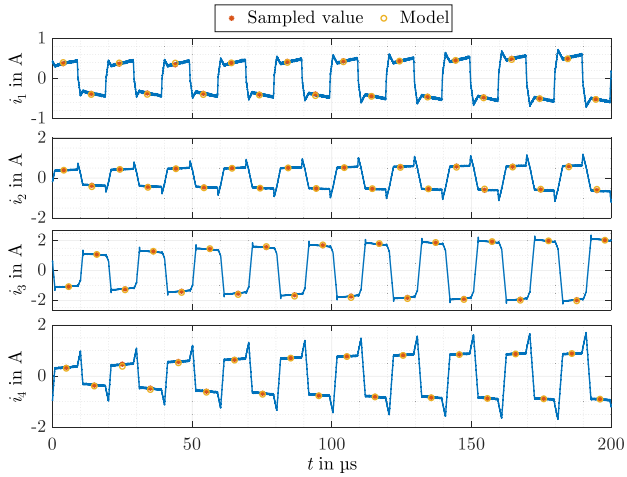

Fig. 31. Comparison of model (yellow circles) and measurement for a step response on a 4-cell MMAB at equal input voltages.

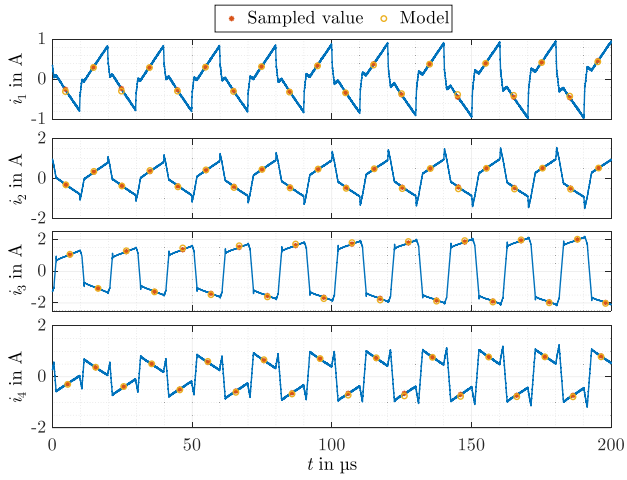

Fig. 32. Comparison of model (yellow circles) and measurement for a step response on a 4-cell MMAB with MAC 1 and 2 in buck-mode.

measurement circuits, as the cells did not include dc-blocking capacitors.

B. MAC-Model Verification on a 4-Cell MMAB

To verify the modeling approach for a more complex system, the MMAB in Fig. 19 is used to test the developed discrete-time state-space model. The transformer is modeled using the parameters given in Tab. II. MAC 1, 2, and 4 are source controlled with K_{P} values of 167 ns/A, MAC 3 is load controlled with an additional K_{I} gain of 8 ns/ε_{I}. The investigation is carried out on a load step from -1 A to -2 A at a dead time of 25 ns to avoid nonlinear effects.

To validate the modeling approach under different scenarios, two cases are evaluated. In Fig. 31, the input voltages are identical (30 V) for all MACs. In Fig. 32, the input voltages of MAC 1 and 2 are increased to 40 V. The parameters are summarized in Table IV.

Since the load current is drawn from multiple sources, the source-side step-response is less pronounced for the MMAB.

TABLE IV
CONTROL PARAMETER SETUP FOR A 4-CELL MMAB

Port m	$K_{\mathrm{P},m}$ in ns/A	$K_{\mathrm{I},m}$ in ns/ε_{I}	V_m in V	$i_{\mathrm{set},m}$ in A
1	167	-	30 (Fig. 31) 40 (Fig. 32)	0
2	167	-	30 (Fig. 31) 40 (Fig. 32)	0
3	167	8	30	-1 $\rightarrow$ -2
4	167	-	30	0

Still, like with the DAB, the model (yellow circles) and sampled measurement (red stars) in Fig. 31 are closely aligned.

In Fig. 32, MAC 1 and 2 operate in buck-mode, leading to increased reactive current flow between all cells. While the reactive current has no effect due to the chosen point of current sampling, the increased input voltages still impact the dynamics of the system. Nevertheless, the developed discrete-time state-space model can be effectively used to predict state progression for the MMAB.

C. Discussion on Model Inaccuracies

In terms of model inaccuracies, besides the aforementioned dead times, the model does not include any resistances. While it is not impossible to introduce these in the model, they would rob the modeling approach of its elegance. The attentive reader might have noticed, that the system developed does not require a fixed timestep between two samplings. While this allows for a linear description of an otherwise truly time variant system – even changing sampling frequency between switching cycles – it makes introduction of resistances only possible, if the system is linearized around an operating frequency. As shown in this Section, this is not required for good model accuracy. We assume, that differences in inductance due to temperature variations in the transformer core will have more of an impact, than internal resistances for stability estimation. In addition, as resistances will limit the rise in current, they should act stabilizing on the system, thereby leading to the engineers erring on the side of caution.

V. DISCUSSION ON USE IN APPLICATIONS

The control scheme introduced in this article allows for the fully decentralized control of active bridges on an arbitrarily large transformer. This opens up a new field of applications, where the amount of active cells was formerly limited by the centralized controller.

An example where MAC control can easily be implemented is the energy router, as introduced in [37], [38]. So far, these need a centralized controller, thereby limiting the amount of possible router ports through controller calculation and sampling limitations, the MAC approach opens up the possibility of near infinite participants on a single magnetically coupled transformer. In this case, the transformer becomes a grid with each cell acting as an individual participant with its own control goals. Here, droop control schemes as introduced for microgrids [65], [66], [67], [68] could be introduced to the MAC. This could enable a full decentralized control of multiple participants on a single transformer. While the equations developed in this article enable the setup of a stable system through necessary stability criteria, sufficient stability criteria – as already implemented in other types of microgrids [69], [70], [71] – might greatly reduce the complexity of setting up a stable system.

Another point not discussed in this article is the efficient operation of multiple cells with wide voltage ranges at a single transformer. The proposed control scheme is an extension of single phase shift between individual cells, which is typically not the most efficient operating mode of MABs with wide voltage ranges. A standard approach would be introducing internal phase shifts at individual ports. These could be set by a centralized controller and handed down to the individual cells through higher level communication. This centralized controller would then play the part of a power management system. Development of a model for the reactive transformer currents at each cell might allow this power management system to use advanced methods like model predictive control, or neural networks to optimize efficiency of the ensemble, as has already been investigated for DABs and MABs [72], [73], [74], [75], [76].

Concerning SSTs, MAC control could potentially fully limit the need for communication between individual cells. This would greatly reduce isolation and communication complexity in MVDC to LVDC SSTs operating in input-serial-output-parallel (ISOP), or potentially even HVDC to MVDC SSTs in input-serial-output-serial (ISOS) configuration. In these serialized configurations, especially the impact of nonsymmetric coupling on the input side needs to be further investigated, as $\bar{i}_a$ needs to be equal at every serialized cell to avoid diverging input voltages. While this can be easily realized for the output of the converter – each cell knows its target voltage – the input voltage necessarily needs to offer some flexibility, when connected to a distributed grid.

In addition, enabling the inclusion of ac ports into power routers or SSTs would further increase the possible range of applications. Direct low-frequency ac coupling to high-frequency transformers has been investigated for various applications in recent years [28], [77], [78], [79], [80]. Since the developed solutions typically include active bridges on the dc side already, they would be valuable additions to MMABs. Still, to allow these solutions to be compatible within the MAC framework, further investigation into the interference between MAC control and the low frequency ac side current or voltage control is necessary, as required power factors and pulsating input voltages could interfere with the communication-less approach presented in this article.

Another possible application of MAC control could be wireless power transfer (WPT). In WPT, sending gate signals between the two cells is nearly impossible, as there is no physical connection. Under typical control schemes, this requires the receiving side to operate as a pure rectifier, thereby having no control on power flow. Implementing MAC control in a WPT application would allow for both cells to control power transfer. This could allow for high dynamic bidirectional wireless charging of EVs, or single-stage power flow control in wireless charging of consumer electronics without the need for overarching wireless communication. As coupling is usually low in WPT, different types of *LC*-resonant converters are used to

increase power transfer capability [81], [82], [83]. The MAC modeling would therefore need to be adapted for these resonant tanks.

VI. Conclusion

This article introduces and analyzes the MAC. The MAC extends single phase shift of a MAB to enable fully decentralized control of multiple converter cells on a single transformer. As slight variations in clock frequency between individual controllers renders setting fixed phase shifts between cells impossible, MAC control uses slight variations in switching frequency to continuously adjust phase shift between cells. Power flow is therefore controlled by the ensemble of individual cells changing their individual switching frequency according to their control law. An MMAB with MAC control therefore behaves very closely like a centrally controlled MAB with single phase shift in terms of efficiency and voltage gain.

To allow for stable readjustment of frequencies, a digital control is developed. The control scheme is introduced step by step with increasing complexity. In the simplest case, each cells MCU samples the transformer current once every switching period, with all cells operating in trapezoidal mode. If the current is sampled at the center of either the positive or negative half-wave in each cell, the system can be represented as a linear discrete time system. This fact can be used to select control parameters based on the eigenvalues of the system. The model is then extended to allow for individual cells to operate with absolute phase shifts larger than $\pi/2$. To also allow for active dc-bias compensation, the control is finally extended to the controller sampling each half-wave. The resulting effects are integrated in the model.

To test the prediction capabilities of the model, MAC control is verified experimentally. The model was able to predict instabilities caused by badly selected control parameters as shown in Section III-B, or specific combinations of cells increasing their phase shift past $\pi/2$ (see Section III-D). As investigated in Section III-E, MAC control allows for the semi-independent control of positive and negative half-waves, thereby eliminating dc-offsets that typically occur in traditional single phase-shift control. For dynamic events, high model accuracy was shown in Section IV for DAB and MAB applications, thereby validating the description of multiple active cells with variable switching frequencies by a simple linear system.

Since this work only introduces the basic control scheme, many open questions remain regarding implementation in various applications. The potential benefits of MAC control along with remaining challenges are therefore discussed for different possible applications like energy routers, SSTs or WPT.

References

[1] P. García-Triviño, J. P. Torreglosa, L. M. Fernández-Ramírez, and F. Jurado, "Control and operation of power sources in a medium-voltage direct-current microgrid for an electric vehicle fast charging station with a photovoltaic and a battery energy storage system," *Energy*, vol. 115, pp. 38–48, Nov. 2016.

[2] P. Garcia-Trivino, J. P. Torreglosa, L. M. Fernandez-Ramirez, and F. Jurado, "Decentralized fuzzy logic control of microgrid for electric vehicle charging station," *IEEE Trans. Emerg. Sel. Topics Power Electron.*, vol. 6, no. 2, pp. 726–737, Jun. 2018.

[3] R. Schwanninger, J. Friedrich, M. Lavery, and M. Maerz, "Investigation of a decentralized energy management system for undersupplied EV charging parks," in *Proc. IEEE 6th Int. Conf. DC Microgrids*. Columbia, SC, USA: IEEE, Aug. 2024, pp. 1–7.

[4] P. T. Krein, "Data center challenges and their power electronics," *CPSS Trans. Power Electron. Appl.*, vol. 2, no. 1, pp. 39–46, Apr. 2017.

[5] D. Rothmund, T. Guillod, D. Bortis, and J. W. Kolar, "99% efficient 10 kV SiC-Based 7 kV/400 v DC transformer for future data centers," *IEEE Trans. Emerg. Sel. Topics Power Electron.*, vol. 7, no. 2, pp. 753–767, Jun. 2019.

[6] T. Babasaki, T. Tanaka, K. Asakura, Y. Nozaki, and F. Kurokawa, "Development of power distribution cabinet for higher-voltage direct-current power feeding system," in *Intelec 2010*. Orlando, FL, USA: IEEE, Jun. 2010, pp. 1–5.

[7] G. Sulligoi, A. Tessarolo, V. Benucci, A. Millerani Trapani, M. Baret, and F. Luise, "Shipboard power generation: Design and development of a medium-voltage dc generation system," *IEEE Ind. Appl. Mag.*, vol. 19, no. 4, pp. 47–55, Jul. 2013.

[8] S. Yousefizadeh, J. D. Bendtsen, N. Vafamand, M. H. Khooban, T. Dragicevic, and F. Blaabjerg, "EKF-Based predictive stabilization of shipboard DC microgrids with uncertain time-varying load," *IEEE Trans. Emerg. Sel. Topics Power Electron.*, vol. 7, no. 2, pp. 901–909, Jun. 2019.

[9] R. Xie and H. Li, "Fault performance comparison study of a dual active bridge (DAB) converter and an isolated modular multilevel DC/DC (iM2DC) converter for power conversion module application in a breakerless shipboard MVDC system," *IEEE Trans. Ind. Appl.*, vol. 54, no. 5, pp. 5444–5455, Sep. 2018.

[10] L. Zheng, R. P. Kandula, and D. Divan, "Current-source solid-state DC transformer integrating LVDC microgrid, energy storage, and renewable energy into MVDC grid," *IEEE Trans. Power Electron.*, vol. 37, no. 1, pp. 1044–1058, Jan. 2022.

[11] T. Dragicevic, J. C. Vasquez, J. M. Guerrero, and D. Skrlec, "Advanced LVDC electrical power architectures and microgrids: A step toward a new generation of power distribution networks," *IEEE Electrific. Mag.*, vol. 2, no. 1, pp. 54–65, Mar. 2014.

[12] C. Moscatiello et al., "A new proposal for power sharing in LVDC energy community microgrids," *IEEE Trans. Ind. Appl.*, pp. 1–11, 2023.

[13] T. Kaipia et al., "Survey of market prospects and standardisation development needs of LVDC technology," *CIRED - Open Access Proc. J.*, vol. 2017, no. 1, pp. 454–458, Oct. 2017.

[14] M. Baran and N. Mahajan, "DC distribution for industrial systems: Opportunities and challenges," *IEEE Trans. Ind. Appl.*, vol. 39, no. 6, pp. 1596–1601, Nov. 2003.

[15] B. Wunder, L. Ott, J. Kaiser, Y. Han, F. Fersterra, and M. Marz, "Overview of different topologies and control strategies for DC micro grids," in *Proc. 2015 IEEE 1st Int. Conf. DC Microgrids*. Atlanta, GA, USA: IEEE, Jun. 2015, pp. 349–354.

[16] J. Hu, M. Stieneker, P. Joebges, and R. W. De Doncker, "Intelligent DC-DC converter based substations enable breakerless MVDC grids," in *Proc. 2018 IEEE Electronic Power Grid*. Charleston, SC: IEEE, Nov. 2018, pp. 1–5.

[17] R. Mencher, J. Mathé, and R. W. De Doncker, "Breaker-less MVDC-Grid with single-phase dual-active bridge," in *Proc. IEEE 10th Int. Power Electron. Motion Control Conf.* Chengdu, China: IEEE, May 2024, pp. 979–983.

[18] S. Marquardt, C. Dahmen, and T. Brückner, "Fault management in meshed MVDC grids enabling uninterrupted operation," in *Proc. PCIM Eur.; Int. Exhib. Conf. Power Electron., Intell. Motion, Renewable Energy, Energy Manage.*, Nuremberg, Germany, 2023, pp. 1–10, doi: 10.30420/566091038.

[19] T. Dragicevic, X. Lu, J. C. Vasquez, and J. M. Guerrero, "DC microgrids—Part II: A review of power architectures, applications, and standardization issues," *IEEE Trans. Power Electron.*, vol. 31, no. 5, pp. 3528–3549, May 2016.

[20] V. A. K. Prabhala, B. P. Baddipadiga, and M. Ferdowsi, "DC distribution systems — An overview," in *Proc. Int. Conf. Renewable Energy Res. Application*. Milwaukee, WI, USA: IEEE, Oct. 2014, pp. 307–312.

[21] L. Mackay, N. H. V. D. Blij, L. Ramirez-Elizondo, and P. Bauer, "Toward the universal DC distribution system," *Electric Power Compon. Syst.*, vol. 45, no. 10, pp. 1032–1042, Jun. 2017.

[22] G. P. Adam, T. K. Vrana, R. Li, P. Li, G. Burt, and S. Finney, "Review of technologies for DC grids–power conversion, flow control and protection," *IET Power Electron.*, vol. 12, no. 8, pp. 1851–1867, Jul. 2019.

[23] S. Kenzelmann, A. Rufer, D. Dujic, F. Canales, and Y. R. De Novaes, "Isolated DC/DC structure based on modular multilevel converter," *IEEE Trans. Power Electron.*, vol. 30, no. 1, pp. 89–98, Jan. 2015.

[24] T. Ericsen and A. Tucker, "Power electronics building blocks and potential power modulator applications," in *Proc. Conf. Rec. Twenty-Third Int. Power Modulator Symp.* Rancho Mirage, CA, USA: IEEE, 1998, pp. 12–15.

[25] D. Boroyevich, "Building block integration in power electronics," in *Proc. IEEE Int. Symp. Ind. Electron.* Bari, Italy: IEEE, Jul. 2010, pp. 3673–3678.

[26] C. Klumpner, P. Nielsen, I. Boldea, and F. Blaabjerg, "New solutions for a low-cost power electronic building block for matrix converters," *IEEE Trans. Ind. Electron.*, vol. 49, no. 2, pp. 336–344, Apr. 2002.

[27] A. Lesnicar and R. Marquardt, "An innovative modular multilevel converter topology suitable for a wide power range," in *Proc. IEEE Bologna Power Tech Conf. Proc.*,, vol. 3. Bologna, Italy: IEEE, 2003, pp. 272–277.

[28] J. E. Huber and J. W. Kolar, "Solid-state transformers: On the origins and evolution of key concepts," *IEEE Ind. Electron. Mag.*, vol. 10, no. 3, pp. 19–28, Sep. 2016.

[29] S. Falcones, R. Ayyanar, and X. Mao, "A DC–DC multiport-converter-based solid-state transformer integrating distributed generation and storage," *IEEE Trans. Power Electron.*, vol. 28, no. 5, pp. 2192–2203, May 2013.

[30] A. A. Faiad, O. M. Hebala, M. S. Hamad, and A. S. Abdel-Khalik, "A modular multilevel converter based solid state transformer (MMC-SST) for high power wind generators," in *Proc. 22nd Int. Middle East Power Syst. Conf.* Assiut, Egypt: IEEE, Dec. 2021, pp. 631–636.

[31] F. Rojas, M. Diaz, M. Espinoza, and R. Cardenas, "A solid state transformer based on a three-phase to single-phase modular multilevel converter for power distribution networks," in *Proc. IEEE Southern Power Electron. Conf.* Puerto Varas, Chile: IEEE, Dec. 2017, pp. 1–6.

[32] M. A. Hannan et al., "State of the art of solid-state transformers: Advanced topologies, implementation issues, recent progress and improvements," *IEEE Access*, vol. 8, pp. 19113–19132, 2020.

[33] C. Gu, Z. Zheng, L. Xu, K. Wang, and Y. Li, "Modeling and control of a multiport power electronic transformer (PET) for electric traction applications," *IEEE Trans. Power Electron.*, vol. 31, no. 2, pp. 915–927, Feb. 2016.

[34] A. K. Bhattacharjee, N. Kutkut, and I. Batarseh, "Review of multiport converters for solar and energy storage integration," *IEEE Trans. Power Electron.*, vol. 34, no. 2, pp. 1431–1445, Feb. 2019.

[35] C. Zhao, S. D. Round, and J. W. Kolar, "An isolated three-port bidirectional DC-DC converter with decoupled power flow management," *IEEE Trans. Power Electron.*, vol. 23, no. 5, pp. 2443–2453, Sep. 2008.

[36] X. Liu, Z. Zheng, K. Wang, and Y. Li, "An energy router based on multi-winding high-frequency transformer," in *Proc. IEEE Appl. Power Electron. Conf. Expo.* Long Beach, CA, USA: IEEE, Mar. 2016, pp. 3317–3321.

[37] Y. Chen, P. Wang, Y. Elasser, and M. Chen, "Multicell reconfigurable multi-input multi-output energy router architecture," *IEEE Trans. Power Electron.*, vol. 35, no. 12, pp. 13210–13224, Dec. 2020.

[38] Y. Chen, P. Wang, H. Li, and M. Chen, "Power flow control in multi-active-bridge converters: Theories and applications," in *Proc. IEEE Appl. Power Electron. Conf. Expo.* Anaheim, CA, USA: IEEE, Mar. 2019, pp. 1500–1507.

[39] H. Tao, A. Kotsopoulos, J. L. Duarte, and M. A. M. Hendrix, "Transformer-coupled multiport ZVS bidirectional DC–DC converter with wide input range," *IEEE Trans. Power Electron.*, vol. 23, no. 2, pp. 771–781, Mar. 2008.

[40] P. Wang, Y. Chen, P. Kushima, Y. Elasser, M. Liu, and M. Chen, "A 99.7% Efficient 300 W hard disk drive storage server with multiport Ac-coupled differential power processing," in *Proc. IEEE Energy Convers. Congr. Expo.* Baltimore, MD, USA: IEEE, Sep. 2019, pp. 5124–5131.

[41] M. Liu, P. Wang, Y. Guan, and M. Chen, "A 13.56 MHz multiport-wireless-coupled (mwc) battery balancer with high frequency online electrochemical impedance spectroscopy," in *Proc. 2019 IEEE Energy Convers. Congr. Expo.* Baltimore, MD, USA: IEEE, Sep. 2019, pp. 537–544.

[42] H. Jeong, H. Lee, Y.-C. Liu, and K. A. Kim, "Review of differential power processing converter techniques for photovoltaic applications," *IEEE Trans. Energy Convers.*, vol. 34, no. 1, pp. 351–360, Mar. 2019.

[43] R. De Doncker, D. Divan, and M. Kheraluwala, "A three-phase soft-switched high-power-density DC/DC converter for high-power applications," *IEEE Trans. Ind. Appl.*, vol. 27, no. 1, pp. 63–73, Jan./Feb. 1991.

[44] S. Islam and F. Khan, "Wireless pulse-width modulation control of power converters using ultra-wideband technology for distributed high-voltage systems," in *Proc. 2024 IEEE Energy Convers. Congr. Expo.* Phoenix, AZ, USA: IEEE, Oct. 2024, pp. 6576–6580.

[45] D. Rothmund, D. Bortis, and J. W. Kolar, "Highly compact isolated gate driver with ultrafast overcurrent protection for 10 kV SiC MOSFETs," *CPSS Trans. Power Electron. Appl.*, vol. 3, no. 4, pp. 278–291, Dec. 2018.

[46] Y. Koyama and T. Isobe, "Current control of modular multilevel converters with phase-shifted PWM using a daisy-chained distributed control system," *IEEJ Trans. Elect. Electron. Eng.*, vol. 14, no. 7, pp. 1095–1104, Jul. 2019.

[47] S. Farzamkia, M. Zhang, H. Zou, A. Vetrivelan, and A. Q. Huang, "MMC based solid state transformer for large-scale distributed PV integration and medium voltage AC/DC interconnection," *IEEE Trans. Power Del.*, vol. 39, no. 4, pp. 2495–2506, Aug. 2024.

[48] H. Wang, S. Yang, H. Chen, X. Feng, and F. Blaabjerg, "Synchronization for an MMC distributed control system considering disturbances introduced by submodule asynchrony," *IEEE Trans. Power Electron.*, vol. 35, no. 12, pp. 12834–12845, Dec. 2020.

[49] F. C. Y. Lee, R. P. Iwens, Y. Yu, and J. E. Triner, "Generalized computer-aided discrete time-domain modeling and analysis of DC-DC converters," *IEEE Trans. Ind. Electron. Control Instrum.*, vol. IECI-26, no. 2, pp. 58–69, May 1979.

[50] C. J. Hsiao, R. B. Ridley, H. Naitoh, and F. C. Lee, "Circuit-oriented discrete-time modeling and simulation for switching converters[1] ," in *Proc. 1987 IEEE Power Electron. Specialists Conf.* Blacksburg, VA, USA: IEEE, Jun. 1987, pp. 167–176.

[51] R.V. Lutz and M. Grötzbach, "Straightforward discrete modelling for power converter systems," in *Proc. IEEE Power Electron. Specialists Conf.* Toulouse, France: IEEE, Jun. 1985, pp. 761–770.

[52] D. Maksimovic and R. Zane, "Small-signal discrete-time modeling of digitally controlled PWM converters," *IEEE Trans. Power Electron.*, vol. 22, no. 6, pp. 2552–2556, Nov. 2007.

[53] M. Lavery, R. Schwanninger, and M. März, "Use-case-Dependent modeling approach for analysis of distributed DC grids," *IEEE Open J. Power Electron.*, vol. 6, pp. 228–242, 2025.

[54] H. Li, K. Wang, J. Fang, W. Chen, and X. Yang, "High-order generalized averaging method for power electronics modeling from DC to above half the switching frequency," *IEEE Trans. Power Electron.*, vol. 40, no. 1, pp. 176–194, Jan. 2025.

[55] D. Costinett, R. Zane, and D. Maksimovic, "Discrete time modeling of output disturbances in the dual active bridge converter," in *Proc. 2014 IEEE Appl. Power Electron. Conf. Expo. - APEC 2014*. Fort Worth, TX, USA: IEEE, Mar. 2014, pp. 1171–1177.

[56] F. Krismer and J. W. Kolar, "Accurate small-signal model for an automotive bidirectional dual active bridge converter," in *Proc. 11th Workshop Control Model. Power Electron.* Zurich, Switzerland: IEEE, Aug. 2008, pp. 1–10.

[57] F. Krismer and J. W. Kolar, "Accurate small-signal model for the digital control of an automotive bidirectional dual active bridge," *IEEE Trans. Power Electron.*, vol. 24, no. 12, pp. 2756–2768, Dec. 2009.

[58] S. Shao et al., "Modeling and advanced control of dual-active-bridge DC–DC converters: A review," *IEEE Trans. Power Electron.*, vol. 37, no. 2, pp. 1524–1547, Feb. 2022.

[59] A. Tong, L. Hang, H.S.-H. Chung, and G. Li, "Using sampled-data modeling method to derive equivalent circuit and linearized control method for dual-active-bridge converter," *IEEE Trans. Emerg. Sel. Topics Power Electron.*, vol. 9, no. 2, pp. 1361–1374, Apr. 2021.

[60] H. Qin and J. W. Kimball, "Closed-loop control of DC–DC dual-active-bridge converters driving single-phase inverters," *IEEE Trans. Power Electron.*, vol. 29, no. 2, pp. 1006–1017, Feb. 2014.

[61] R. Erickson and D. Maksimovic, "A multiple-winding magnetics model having directly measurable parameters," in *Proc. PESC 98 Record. 29th Annu. IEEE Power Electron. Specialists Conf.*, vol. 2. Fukuoka, Japan: IEEE, 1998, pp. 1472–1478.

[62] B. Zhang, S. Shao, L. Chen, X. Wu, and J. Zhang, "Steady-state and transient DC magnetic flux bias suppression methods for a dual active bridge converter," *IEEE Trans. Emerg. Sel. Topics Power Electron.*, vol. 9, no. 1, pp. 744–753, Feb. 2021.

[63] Q. Bu, H. Wen, H. Shi, and Y. Zhu, "A comparative review of high-frequency transient DC bias current mitigation strategies in dual-active-bridge DC–DC converters under phase-shift modulations," *IEEE Trans. Ind. Appl.*, vol. 58, no. 2, pp. 2166–2182, Mar. 2022.

[64] B. Zhao, Q. Song, W. Liu, and Y. Zhao, "Transient DC bias and current impact effects of high-frequency-isolated bidirectional DC–DC converter in practice," *IEEE Trans. Power Electron.*, vol. 31, no. 4, pp. 3203–3216, Apr. 2016.

[65] L. Ott et al., "An advanced voltage droop control concept for grid-tied and autonomous DC microgrids," in *Proc. IEEE Int. Telecommun. Energy Conf.* Osaka, Japan: IEEE, Oct. 2015, pp. 1–6.

[66] R. Schwanninger, J. Friedrich, K. Drexler, M. Lavery, and M. Maerz, "Introduction of a self-stabilizing decentralized energy management system for undersupplied EV charging parks," *IEEE Open J. Power Electron.*, vol. 6, pp. 660–680, 2025.

[67] R. Wang, Q. Sun, W. Hu, Y. Li, D. Ma, and P. Wang, "SoC-Based droop coefficients stability region analysis of the battery for stand-alone supply systems with constant power loads," *IEEE Trans. Power Electron.*, vol. 36, no. 7, pp. 7866–7879, Jul. 2021.
[68] X. Yang, S. Pohlenz, R. Schwanninger, N. Schleippmann, B. Wunder, and M. März, "Modelling and design of a droop-based cascaded controller for LLC resonant converter," in *Proc. IEEE Fifth Int. Conf. DC Microgrids*. Auckland, New Zealand: IEEE, Nov. 2023, pp. 1–6.
[69] C. Zhang, M. Molinas, A. Rygg, and X. Cai, "Impedance-based analysis of interconnected power electronics systems: Impedance network modeling and comparative studies of stability criteria," *IEEE Trans. Emerg. Sel. Topics Power Electron.*, vol. 8, no. 3, pp. 2520–2533, Sep. 2020.
[70] B. He, W. Chen, X. Ruan, X. Zhang, Z. Zou, and W. Cao, "A generic small-signal stability criterion of DC distribution power system: Bus node impedance criterion (BNIC)," *IEEE Trans. Power Electron.*, vol. 37, no. 5, pp. 6116–6131, May 2022.
[71] A. Riccobono and E. Santi, "Comprehensive review of stability criteria for DC distribution systems," in *Proc. IEEE Energy Convers. Congr. Expo.* Raleigh, NC, USA: IEEE, Sep. 2012, pp. 3917–3925.
[72] A. Nardoto et al., "Enhanced efficiency on ANPC-DAB through adaptive model predictive control," *Energies*, vol. 17, no. 1, Dec. 2023, Art. no. 12.
[73] D. Mou et al., "Reactive power minimization for modular multi-active-bridge converter with whole operating range," *IEEE Trans. Power Electron.*, vol. 38, no. 7, pp. 8011–8015, Jul. 2023.
[74] Y. Tang et al., "Reinforcement learning based efficiency optimization scheme for the DAB DC–DC converter with triple-phase-shift modulation," *IEEE Trans. Ind. Electron.*, vol. 68, no. 8, pp. 7350–7361, Aug. 2021.
[75] L. Chen et al., "Moving discretized control set model-predictive control for dual-active bridge with the triple-phase shift," *IEEE Trans. Power Electron.*, vol. 35, no. 8, pp. 8624–8637, Aug. 2020.
[76] S. M. Akbar, A. Hasan, A. J. Watson, and P. Wheeler, "Model predictive control with triple phase shift modulation for a dual active bridge DC-DC converter," *IEEE Access*, vol. 9, pp. 98603–98614, 2021.
[77] J. Everts, F. Krismer, J. Van Den Keybus, J. Driesen, and J. W. Kolar, "Optimal ZVS modulation of single-phase single-stage bidirectional DAB AC–DC converters," *IEEE Trans. Power Electron.*, vol. 29, no. 8, pp. 3954–3970, Aug. 2014.
[78] J. Saha, N. B. Y. Gorla, A. Subramaniam, and S. K. Panda, "Analysis of modulation and optimal design methodology for half-bridge matrix-based dual-active-bridge (MB-DAB) AC–DC converter," *IEEE Trans. Emerg. Sel. Topics Power Electron.*, vol. 10, no. 1, pp. 881–894, Feb. 2022.
[79] J. Saha, N. B. Yadav Gorla, and S. K. Panda, "Analytical expression-based modulation for soft-switched matrix-based dual-active-bridge (S2MB-DAB) single-phase AC-DC converter," *IEEE Trans. Emerg. Sel. Topics Power Electron.*, vol. 10, no. 6, pp. 6511–6522, Dec. 2022.
[80] J. Saha, N. B. Y. Gorla, and S. K. Panda, "Implementation of power balance control scheme for a cascaded matrix-based dual-active-bridge (CMB-DAB) MVAC-LVDC converter," *IEEE Trans. Ind. Appl.*, vol. 58, no. 1, pp. 388–399, Jan. 2022.
[81] Z. Zhang, H. Pang, A. Georgiadis, and C. Cecati, "Wireless Power Transfer—An Overview," *IEEE Trans. Ind. Electron.*, vol. 66, no. 2, pp. 1044–1058, Feb. 2019.
[82] V. Shevchenko, O. Husev, R. Strzelecki, B. Pakhaliuk, N. Poliakov, and N. Strzelecka, "Compensation topologies in IPT systems: Standards, requirements, classification, analysis, comparison and application," *IEEE Access*, vol. 7, pp. 120559–120580, 2019.
[83] D. Patil, M. K. McDonough, J. M. Miller, B. Fahimi, and P. T. Balsara, "Wireless power transfer for vehicular applications: Overview and challenges," *IEEE Trans. Transport. Electrific.*, vol. 4, no. 1, pp. 3–37, Mar. 2018.

Raffael Schwanninger (Student Member, IEEE) was born in Linz, Austria in 1993. He received the B.Sc. and M.Sc. degrees in electrical engineering, electronics, and information technology from Friedrich-Alexander-University Erlangen-Nuremberg (FAU), Erlangen, Germany, in 2018 and 2020, respectively.

From 2015 to 2019, he was a Working Student with Valeo-Siemens eAutomotive, Erlangen, Germany. Since 2021, he has been with the Institute of Power Electronics, FAU. His research interests include control of power converters, impedance measurement, and dc microgrids.

Niklas Stöcklein received the bachelor's degree in mechatronics from the DHBW Mosbach, Germany, in 2022, a university of applied sciences with a dual studies program in cooperation with Robert Bosch GmbH Bamberg, Germany, and the master's degree from the Friedrich-Alexander University of Erlangen-Nürnberg (FAU), Erlangen, Germany, in 2025. He completed an apprenticeship as a mechatronics technician with Robert Bosch GmbH Bamberg, Germany, in 2019. In the summer of 2024, he did an internship with Hitachi Energy Research, Västerås, Sweden. Since 2025, he has been with the Institute of Power Electronics, FAU. His research interests include modular power electronics and multiwinding transformers, galvanically isolated dc-dc converters and the thermal management of power electronics.

Nikolai Weitz received the B.Sc. and the M.Sc. degrees in electrical engineering from the University of Erlangen-Nuremberg (FAU), Erlangen, Germany, in 2017 and 2019, respectively. He is currently working toward the Ph.D. degree in electrical engineering with the Chair of Power Electronics, FAU.

His research interests include the design, magnetic integration, and control of radio frequency power converters.

Xiaotian Yang was born in Liaoning, China. He received the B.Sc. degree from North China Electric Power University (NCEPU) and The University of Manchester, in 2015, and the M.Sc. degree from RWTH Aachen University, Aachen, Germany, in 2020, all in electrical engineering.

Since 2020, he has been working as a Research Associate in the DC Grid group of the Fraunhofer Institute for Integrated Systems and Device Technology IISB. His research interests include the control of power converters, resonant converters, as well as the control of dc microgrids.

Martin März received the Ph.D. degree in electrical engineering from Friedrich-Alexander-Universität Erlangen-Nürnberg (FAU), in 1995.

After five years at Siemens Semiconductors (later Infineon AG), he became Head of the Power Electronics System Department with the Fraunhofer Institute of Integrated Systems and Device Technology IISB in Erlangen. Since 2012, he has been the deputy Director of the IISB, from 2018 to 2021 Acting Director. In 2016, he was appointed as a Full Professor to the newly established Institute for Power Electronics at the FAU. A particular focus is on mechatronic 3-D system integration and thermal management for applications with harsh environmental conditions (e.g., with cryogenic cooling). His research interests are innovative technologies for improving power density, efficiency, lifetime, and functionality of power electronics.

Dr. März is inventor on more than 100 patents in 40 families and (co-)author on more than 250 scientific papers.